

Chapter 2

Multi-shell Radially Symmetrical Lens Antennas

Zvonimir Sipus and Tin Komljenovic

Abstract In this chapter, we review several aspects of the analysis and the design of multi-shell spherical and circular cylindrical lens antennas. Such lens antennas are attractive for implementation in communication and radar systems, in particular in the millimeter-wave frequency band, due to their broadband behavior, excellent focusing properties, possibility of beam scanning, and the ability to form multiple beams. In order to develop an efficient analysis tool, needed for successful design of multi-shell lens antennas, we first demonstrate the principles of the analysis algorithm for calculating the EM field distribution in general multilayer structures (i.e., inside a structure with an arbitrary number of layers). This algorithm is designed for spherical and circular-cylindrical geometries with elementary excitation. To model realistic lens antennas, we introduce additional flexibility that allows the analysis of actual feed antennas that usually do not follow the symmetry properties of the lens. Finally, by connecting the algorithm with an optimization subroutine, a powerful analysis and design tool is created. All the aspects of the proposed analysis approach are explained and illustrated with examples. Furthermore, some practical problems which are encountered in the design of these types of lens antennas are highlighted and common solutions are presented and compared to the ideal situations.

Z. Sipus (✉)

Faculty of Electrical Engineering and Computing, University of Zagreb,
Unska 3, HR-10000 Zagreb, Croatia
e-mail: zvonimir.sipus@fer.hr

T. Komljenovic

Department of Electrical and Computer Engineering, University of California,
Santa Barbara, CA 93106, USA

2.1 Introduction

In recent years, there is a growing interest for antennas in communication and radar systems at higher microwave and millimeter-wave frequencies. Different kinds of spherical and cylindrical lens antennas are attractive solutions for such applications due to their focusing properties, capability of beam scanning, ability to form multiple beams, and broadband behavior. Furthermore, the typical problems with microwave lenses in the past, such as their bulkiness and weight are no longer an obstacle for practical implementation since by moving to higher frequencies and by using novel materials the size and weight have been considerably reduced. This added degree of freedom in terms of weight and size has in many cases led to the increase in the electrical size of the lenses in order for them to meet requirements for more demanding applications. In addition, the feed can be any type of antenna (horn, dipole, microstrip patch), and typically it is a part of the mechanical system that points the main beam in the desired direction. Altogether, the lens antenna system is a complex electromagnetic design problem that requires efficient and accurate analysis tools that can take into account various practical problems and demands.

The inhomogeneous lenses have first been analysed and designed using geometrical optics and ray-tracing techniques [1–4]. However, these are approximate methods valid for structures with all the dimensions large compared to the wavelength. Furthermore, they cannot take into account internal reflections. The general numerical methods, such as the finite difference time domain [5] or the finite element method in [6], can be applied to the lens analysis. However, such methods are suitable for structures having limited electric dimensions, usually not more than 20 free space wavelengths, and are time- and memory-consuming. Therefore, there is a need for specialized software in which the geometrical properties of the considered structures are analytically taken into account, and which can be efficiently connected with an optimization routine.

The analytical solution for spherical and circular-cylindrical multilayer structures is derived from the solution of the homogeneous Helmholtz equation, known as Mie series. It has been extensively used and reported for plane wave scattering by a conducting and dielectric sphere [7, 8]. This approach has been generalized for multilayered dielectric lens using different formulations: Mie series augmented matrix solution [9, 10], scalar potentials [11], mode matching technique [12–15] or dyadic Green functions [16–19]. The similar analysis approach can be applied for analyzing other types of structures (e.g., conformal microstrip antennas [20–23]).

2.2 Analysis of Spherical and Circular Cylindrical Multilayer Structures

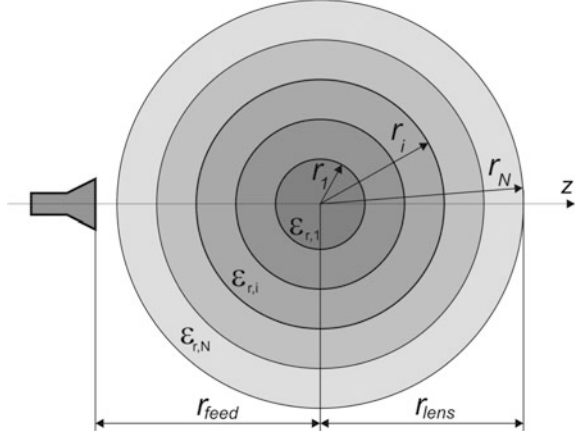
For many structures and technical problems, one requires the knowledge of the field distribution scattered and/or inside multilayer spherical or cylindrical structures. Examples would be lens antennas, radomes, optical fibers, geophysical probing, scattering reduction structures (cloaking), etc. In all the considered cases we would like to determine the EM field distribution inside and around the multilayer structure while the position and/or existence of the source can be arbitrary. For example, in scattering problems the sources are faraway from the structure, in waveguide problems we search for eigenmode solutions, while in the antenna problems the sources are a part of the structure. In general, all of these problems can be described using the Green's function approach, i.e., we can consider the physical or equivalent sources as a part of the structure (the waveguide problems can be treated as poles of the Green's functions). The knowledge of the most appropriate Green's function is often essential for implementing the numerical method we would like to apply. For example, planar, cylindrical, and spherical patch antennas and periodic surfaces are frequently analysed by means of the electric field integral equation and the moment method. There the kernel of the integral operator is a Green's function, which takes into account the considered curved multilayer structure.

2.2.1 *Green's Functions for Layered Media*

In principle, there are two basic approaches for calculating the Green's function of a general multilayer structure: either to analytically derive an expression for it and then code this expression, or to develop a numerical routine for the complete calculation. The analytic approach requires less computer resources than the numerical approach; however, it is very laborious to analytically determine the Green's functions for structures with more than two layers. In such cases, it is more convenient to use a numerical algorithm which determines the Green's function directly. Furthermore, the analytic approach often requires a new derivation of the Green's functions for practically every slightly different problem, such as for different number of layers or for different source locations inside the layers.

In most cases, lenses follow spherical or cylindrical geometry, or a slight variation of these. Therefore, it is reasonable to focus our attention on these geometries and use the inherent properties of these structures to our advantage. Ideal planar, circular cylindrical, and spherical multilayer structures have one property in common: the structure is homogeneous in two dimensions, and varies in the third dimension. For example, the spherical structure in Fig. 2.1 varies in r direction and is homogeneous in θ and ϕ directions. Thus, planar, cylindrical and spherical structures can be referred to as one-dimensional structures since they vary only in

Fig. 2.1 Spherical lens antenna illuminated by a horn antenna



one dimension [24]. We can simplify the problem of determining the field distribution Green's functions for one-dimensional structures if we perform the two-dimensional (2D) Fourier transformation in the coordinates for which the structure is homogeneous. As a result, our original three-dimensional problem is transformed into a series of one-dimensional problems, which are much easier to solve. Instead of using Fourier transformation one can search for modal representation of the EM field, which at the end gives the same EM field expression.

When determining the Green's functions of multilayer one-dimensional structures one can select two paths. The first is to select one component of electric and magnetic potential and then to express the field components at the boundaries to determine the considered potentials. In practice, the algorithm determines the reflection and transmission coefficients of TE and TM waves which are connected (simply by multiplication) in a final matrix that describes the structure (see, e.g., [16]). For example, in the spherical case we can use the Debye potentials ψ_e and ψ_m to characterize the TM and TE waves (note that $\mathbf{r} = r\hat{r}$)

$$\mathbf{E}^{TE} = \nabla \times \mathbf{r}\psi_m \quad (2.1a)$$

$$\mathbf{H}^{TM} = \nabla \times \mathbf{r}\psi_e \quad (2.1b)$$

The Debye potentials ψ_e and ψ_m are determined by solving the scalar Helmholtz differential equation (in spherical coordinate system in this case)

$$\psi_{mn} = z_n(kr)P_n^m(\cos \theta)e^{im\phi} \quad (2.2)$$

Here ψ_n is the elementary solution of the Helmholtz differential equation, i.e., $P_n^m(\cos \theta)$ are the associated Legendre functions of the first kind and z_n denotes spherical Bessel j_n or Hankel $h_n^{(2)}$ functions. Using the following notation:

$$\mathbf{M}_{mn} = \nabla \times \mathbf{r} / r_{mn} \quad (2.3a)$$

$$\mathbf{N}_{mn} = \frac{1}{k} \nabla \times \mathbf{M}_{mn} \quad (2.3b)$$

we can express the electromagnetic field as

$$\mathbf{E} = - \sum_n \sum_m a_{mn} \mathbf{M}_{mn} + b_{mn} \mathbf{N}_{mn}. \quad (2.4a)$$

$$\mathbf{H} = - \frac{j}{\eta} \sum_n \sum_m b_{mn} \mathbf{M}_{mn} + a_{mn} \mathbf{N}_{mn}. \quad (2.4b)$$

The coefficients are determined by fulfilling the boundary conditions for the tangential EM field components (e.g., for electric field)

$$\begin{aligned} \mathbf{E}^{\text{tan}} = & - \sum_{n=0}^{\infty} \sum_{|m| \leq n} \left[a_{nm}^j j_n(kr) + a_{nm}^h h_n^{(2)}(kr) \right] \left(\hat{\theta} \frac{jm}{\sin \theta} P_n^{|m|}(\cos \theta) - \hat{\phi} \frac{d}{d\theta} P_n^{|m|}(\cos \theta) \right) e^{jm\phi} \\ & + \frac{1}{kr} \frac{d}{dr} \left[b_{nm}^j r j_n(kr) + b_{nm}^h r h_n^{(2)}(kr) \right] \left(\hat{\theta} \frac{d}{d\theta} P_n^{|m|}(\cos \theta) + \hat{\phi} \frac{jm}{\sin \theta} P_n^{|m|}(\cos \theta) \right) e^{jm\phi} \end{aligned} \quad (2.5)$$

By fulfilling the boundary conditions at each boundary (continuity of the tangential components) the reflection coefficients can be determined, see [16] for details.

The second approach is based on determining the tangential components of the EM field (so-called propagator matrix approach [16]). This approach actually corresponds to the implementation of the Huygens's principle or more precisely, the Love's equivalence theorem [8]. Here the original problem is divided into equivalent subproblems, one for each layer. The field inside each layer is then determined from equivalent currents at the subproblem boundaries and from the sources inside that subproblem. As a theoretical background, in parallel to the Love's equivalence theorem, we can modify the curl Maxwell's equation to "eliminate" the normal component of the EM field, i.e., to get the equations that depend only on the tangential field and source components. This modification is given in [25] and the resulting equations are (e.g., for H-field; by duality principle the equivalent equation can be derived for the E-field)

$$\begin{aligned} - \frac{\partial}{\partial n} \mathbf{H}_t &= \frac{j\eta}{k} \left(1 + \frac{\nabla_t \nabla_t}{k^2} \right) \cdot (\hat{n} \times \mathbf{E}_t) + \hat{n} \times \mathbf{J}_{te} \\ \mathbf{J}_{te} &= \mathbf{J}_t - \frac{j}{\eta k} \nabla \times \mathbf{M}_n \end{aligned} \quad (2.6)$$

Here subscripts t and n denote tangential and normal directions (related to the considered boundary), \hat{n} is the unit vector in the normal direction, and ∇_t is the transverse part of the ∇ operator. In other words, in order to determine the EM fields inside the considered multilayer structure we need to know the tangential EM field components at each boundary as well as tangential component of the excitation currents inside the structure. Note that the excitation current in Eq. (2.6) contains two parts: the tangential electric current J_t and the replacement tangential electric current with the origin in the normal component of the excitation magnetic current M_n .

2.2.2 Description of the G1DMULT Algorithm

As indicated, a canonical three-dimensional problem can be efficiently decomposed into one-dimensional subproblems by applying Fourier transformation for the directions where the structure is homogeneous. This so-called spectral domain approach is the core of an algorithm called G1DMULT for calculating the Green's function in the spectral domain (representing a one-dimensional (1D) spatial domain) for planar, circular cylindrical, and spherical multilayer structures. The G1DMULT algorithm calculates the Green's functions in the same way for all three types of geometries and it will be explained by considering the spherical geometry.

The solution procedure makes use of the Fourier transformation technique. Since the problem is described in spherical coordinate system, we use the vector Legendre transformation in θ and ϕ directions, defined by [26, 24].

$$\tilde{\mathbf{J}}(r, n, m) = \frac{1}{\sqrt{2\pi S(n, m)}} \int_{-\pi}^{\pi} \int_0^{\pi} \tilde{\mathbf{L}}(n, m, \theta) \mathbf{J}(r, \theta, \phi) \sin \theta e^{-jm\phi} d\theta d\phi \quad (2.7a)$$

$$\mathbf{J}(r, \theta, \phi) = \sum_{m=-\infty}^{\infty} \sum_{n=|m|}^{\infty} \frac{1}{\sqrt{2\pi S(n, m)}} \tilde{\mathbf{L}}(n, m, \theta) \tilde{\mathbf{J}}(r, n, m) e^{jm\phi} \quad (2.7b)$$

$$\tilde{\mathbf{L}}(n, m, \theta) = \begin{bmatrix} P_n^{|m|}(\cos \theta) \sqrt{n(n+1)} & 0 & 0 \\ 0 & \frac{\partial P_n^{|m|}(\cos \theta)}{\partial \theta} & \frac{-jm P_n^{|m|}(\cos \theta)}{\sin \theta} \\ 0 & \frac{jm P_n^{|m|}(\cos \theta)}{\sin \theta} & \frac{\partial P_n^{|m|}(\cos \theta)}{\partial \theta} \end{bmatrix} \quad (2.7c)$$

$$S(n, m) = \frac{2n(n+1)(n+|m|)!}{(2n+1)(n-|m|)!}. \quad (2.7d)$$

By applying the vector Legendre transformation, the three-dimensional excitations are transformed into harmonic current shells. If the source is infinitely thin in r direction, we get one discrete current shell per source, otherwise we get a

continuous distribution of current shells in r direction. The E- and H-fields induced by the harmonic current sources have the same harmonic variations in θ and ϕ as the source. Therefore, only the field variation in the direction perpendicular to the boundaries is unknown, and we have a harmonic one-dimensional (1D) field problem. In this way, the spectral domain problem is interpreted as a one-dimensional spatial domain problem consisting of one-dimensional multilayer structure and harmonic one-dimensional sources in the form of current shells. This is visualized in Fig. 2.2, where also all other steps of the algorithm are shown. We describe the steps of the algorithm below.

The harmonic one-dimensional problem is solved by making use of the equivalent problems, one for each layer. The unknowns are the tangential E- and H-fields at layer boundaries. Since the variation of the E- and H-fields in the direction tangential to the boundaries is harmonic with known periodicity, we only need to determine the complex field amplitudes at the interfaces, i.e., we have four unknowns per boundary. For example, the E-field in the layer j is expressed as

$$\tilde{\mathbf{E}}_j = \tilde{\mathbf{G}}_{EJ}^{\text{homo}} \tilde{\mathbf{J}}_{j-1} + \tilde{\mathbf{G}}_{EJ}^{\text{homo}} \tilde{\mathbf{J}}_j + \tilde{\mathbf{G}}_{EM}^{\text{homo}} \tilde{\mathbf{M}}_{j-1} + \tilde{\mathbf{G}}_{EM}^{\text{homo}} \tilde{\mathbf{M}}_j + \tilde{\mathbf{G}}_{EJ}^{\text{homo}} \tilde{\mathbf{J}}_j^{\text{exci}} + \tilde{\mathbf{G}}_{EM}^{\text{homo}} \tilde{\mathbf{M}}_j^{\text{exci}}, \quad (2.8)$$

where $\tilde{\mathbf{J}}_j$ and $\tilde{\mathbf{M}}_j$ are equivalent electric and magnetic current sheets at boundary j , $\tilde{\mathbf{J}}_j^{\text{exci}}$ and $\tilde{\mathbf{M}}_j^{\text{exci}}$ are excitation electric and magnetic currents in layer j (if any), and $\tilde{\mathbf{G}}_{\text{homo}}$ is the Green's function of the homogeneous problem (given below). By using $\tilde{\mathbf{J}}_j = \hat{n} \times \tilde{\mathbf{H}}_j$ and $\tilde{\mathbf{M}}_j = -\hat{n} \times \tilde{\mathbf{E}}_j$ Eq. (2.8) can be expressed in terms of the unknown EM field amplitudes $\tilde{\mathbf{E}}_j$ and $\tilde{\mathbf{H}}_j$ at the boundary j between layers j and $j+1$ and the known excitation currents. Since the tangential E- and H-fields are continuous at the layer boundaries we obtain 4 linear equations per boundary.

The algorithm connects all equivalent subproblems into a system of $4N_{\text{boundary}}$ linear equations with the same number of unknowns (N_{boundary} denotes the number of boundaries). Once the amplitudes of the tangential fields have been determined, it is easy to determine the field amplitudes anywhere in the multilayer structure by applying the homogeneous region equivalent of the layer inside which we want to determine the field value.

The core subproblem in the formulation is to calculate the E- and H-fields due to a harmonic current shell excitation of radius r_s in a homogeneous region. This is the only part (i.e., the only subroutine) that is different for planar, cylindrical and spherical case. In the spherical case the formulation is as follows:

(a) from $\tilde{J}_\theta(r_s, m, n)$

$$\tilde{E}_\theta(r, n, m) = -\frac{k}{\omega \epsilon} \frac{r_s}{r} \tilde{J}_\theta(n, m) \cdot \begin{cases} \hat{H}_n^{(2)'}(kr_s) \hat{J}_n'(kr) & r \leq r_s \\ \hat{J}_n'(kr_s) \hat{H}_n^{(2)'}(kr) & r \geq r_s \end{cases} \quad (2.9a)$$

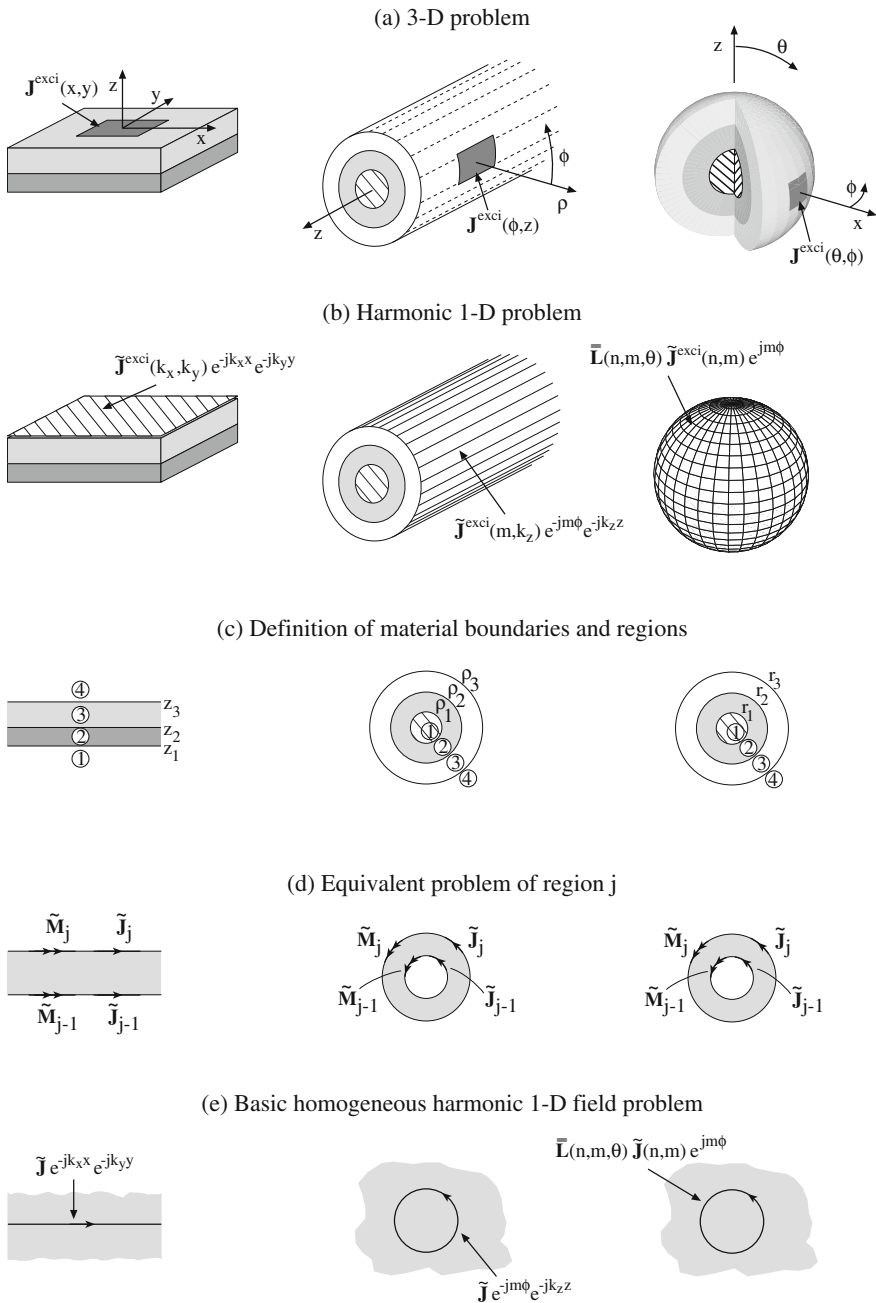


Fig. 2.2 Structure of the G1DMULT algorithm

$$\tilde{E}_r(r, n, m) = -\frac{1}{\omega \epsilon} \frac{r_s}{r^2} \sqrt{n(n+1)} \tilde{J}_0(n, m) \cdot \begin{cases} \hat{H}_n^{(2)}(kr_s) \hat{J}_n(kr) & r \leq r_s \\ \hat{J}_n(kr_s) \hat{H}_n^{(2)}(kr) & r \geq r_s \end{cases} \quad (2.9b)$$

$$\tilde{H}_\phi(r, n, m) = \frac{j r_s}{r} \tilde{J}_0(n, m) \cdot \begin{cases} \hat{H}_n^{(2)}(kr_s) \hat{J}_n(kr) & r \leq r_s \\ \hat{J}_n(kr_s) \hat{H}_n^{(2)}(kr) & r \geq r_s \end{cases} \quad (2.9c)$$

(b) from $\tilde{J}_\phi(r_s, m, n)$

$$\tilde{E}_\phi(r, n, m) = -\frac{k}{\omega \epsilon} \frac{r_s}{r} \tilde{J}_\phi(n, m) \cdot \begin{cases} \hat{H}_n^{(2)}(kr_s) \hat{J}_n(kr) & r \leq r_s \\ \hat{J}_n(kr_s) \hat{H}_n^{(2)}(kr) & r \geq r_s \end{cases} \quad (2.10a)$$

$$\tilde{H}_\theta(r, n, m) = \frac{j r_s}{r} \tilde{J}_\phi(n, m) \cdot \begin{cases} \hat{H}_n^{(2)'}(kr_s) \hat{J}_n'(kr) & r \leq r_s \\ \hat{J}_n'(kr_s) \hat{H}_n^{(2)'}(kr) & r \geq r_s \end{cases} \quad (2.10b)$$

$$\tilde{H}_r(r, n, m) = \frac{j r_s}{kr^2} \sqrt{n(n+1)} \tilde{J}_\phi(n, m) \cdot \begin{cases} \hat{H}_n^{(2)}(kr_s) \hat{J}_n(kr) & r \leq r_s \\ \hat{J}_n(kr_s) \hat{H}_n^{(2)}(kr) & r \geq r_s \end{cases} \quad (2.10c)$$

Here $\hat{J}_n(kr)$ and $\hat{H}_n^{(2)}(kr)$ are the Schelkunoff type of spherical Bessel and Hankel functions ($\hat{J}_n(x) = x j_n(x)$ and $\hat{H}_n^{(2)}(x) = x h_n^{(2)}(x)$), and k is the wave number of the considered layer. The fields excited by the magnetic shell can easily be determined by applying the duality concept. The fields caused by the r -directed sources are evaluated using the transverse replacement currents (see [24] for details).

Once we have the fields inside the structure the procedure to obtain the radiation pattern is quite straightforward. If we consider, e.g., the ϕ -component of the electric field in the outermost region with the r -coordinate larger than the r -coordinate of the patch, we have only outward-traveling waves described by $a_{nm}^i \hat{H}_n^{(2)}(k_0 r)$. Therefore, in the outermost region we can connect the ϕ -component of the electric field with different r -coordinates r_1 and r_2 as

$$\tilde{E}_\phi(r_1, n, m) = \tilde{E}_\phi(r_2, n, m) \frac{r_2 \hat{H}_n^{(2)}(k_0 r_1)}{r_1 \hat{H}_n^{(2)}(k_0 r_2)} \approx \tilde{E}_\phi(r_2, n, m) \frac{j^{n+1} r_2}{\hat{H}_n^{(2)}(k_0 r_2)} \frac{\exp(-jk_0 r_1)}{r_1} \quad (2.11a)$$

$$\tilde{E}_\theta(r_1, n, m) = \tilde{E}_\theta(r_2, n, m) \frac{r_2 \hat{H}_n^{(2)'}(k_0 r_1)}{r_1 \hat{H}_n^{(2)'}(k_0 r_2)} \approx \tilde{E}_\theta(r_2, n, m) \frac{j^n r_2}{\hat{H}_n^{(2)'}(k_0 r_2)} \frac{e^{-jk_0 r_1}}{r_1} \quad (2.11b)$$

Here r_l represents the r -coordinate of the far-field pattern. This avoids the problem of evaluating Hankel functions with very large argument. Notice that in the lens analysis a slightly larger value than the feed position is chosen for the radius r_2 . The final solution is obtained by superposing the spectral solutions, see Eqs. (2.7a–2.7d).

In order to calculate the directivity radiation pattern it is necessary to calculate the radiated power. This is done in spectral domain by using Parseval theorem [8], i.e., the radiated power is equal

$$P^{rad} = r_2^2 \operatorname{Re} \left[\sum_{\forall m} \sum_{n \geq |m|} S(n, m) (\tilde{E}_\theta \tilde{H}_\phi^* - \tilde{E}_\phi \tilde{H}_\theta^*) \right]. \quad (2.12)$$

To summarize, the presented modal analysis approach (i.e., the spectral domain approach or the Mie series approach) is completely rigorous (there are no approximations in the formulation) and suitable for analyzing lenses with arbitrary number of layers. However, its application is limited only to canonical geometries (spherical, circular-cylindrical or planar) and one should be aware that numerical problems can appear for electrically very large structures. Two major sources of possible numerical difficulties are connected with the problem of the associated Legendre functions $P_n^m(\cos \theta)$ becoming very large (especially if $m \approx n$, $P_n^{|m|}(\cos \theta) \sim n^{|m|-1/2|}$, making the solution numerically unstable), and with the problem of calculating Bessel/Hankel functions of large order. The first numerical difficulty linked to associated Legendre functions can be solved using suitable normalization process [22]. The second numerical problem (Bessel/Hankel functions of large order) can be mitigated by implementing the Debye's asymptotic formulas for Bessel and Hankel functions of large order, by which either the product of Bessel and Hankel function, or the ratio of two Hankel functions, are calculated with extracted exponential parts [22].

Multilayer canonical one-dimensional structures can also be analyzed by expressing the field quantities inside each layer as the superposition of forward and backward propagating waves (as mentioned at the beginning of this chapter). The reflection and transmission coefficients inside each layer can be determined in a recursive way, resulting in the generalized reflection and transmission coefficient of the whole structure (i.e., of the generalized scattering matrix). A detailed description of this method is given in [16]. Although in the presented approach the forward and backward propagating waves are also considered, the way of determining the field quantities is different—the presented G1DMULT algorithm simultaneously determines the tangential field quantities at the interfaces between the layers. Unlike in [16], in the presented method the field solutions to all the subproblems in the procedure are given in terms of Green's functions, i.e., the excitation within each subproblem are equivalent or physical current sources. This makes it easy to modify the code. For example, it is easy to implement the metasurface impedance boundary

conditions into the routine, which makes the algorithm suitable for analyzing multilayer metasurface structures (e.g., metasurface lenses).

2.3 Spherical Multi-shell Lenses

Spherical lens antennas in general have many attractive features like broadband behavior, excellent focusing properties, wide scan coverage without scanning losses, possibilities of multiple beams on (in general) different working frequencies, etc. Such properties make lens antennas attractive solution in many applications, in particular in millimeter frequency range where the weight of such antennas is no longer an obstacle for practical implementation due to the increased frequency of operation. Two most common designs follow the spherical Luneburg and half Maxwell fisheye variation of index of refraction (see Fig. 2.3 and [27]), i.e., the respective radial dependency of index of refractive is equal

$$n^2(r) = 2 - r^2 \quad \text{and} \quad n^2(r) = 4 / (1 + r^2)^2. \quad (2.13)$$

For example, spherical lens antennas can be used for automotive radars [28], radar cross-section (RCS) enhancers [29], satellite communications [30, 31], or for astronomy applications [32].

2.3.1 Modeling of Feed Antennas

As explained in the previous section, spherical lens antennas are usually rigorously analysed using spherical wave decomposition. However, the feed was usually taken only in an approximate way. For example, the Huygens source (approximation of low-gain horns) was considered in [10], dipole sources were considered in [17], and in [12, 13] the feeding horn antenna was modeled by an array of dipoles representing the aperture field distribution of the horn. In more details, in the case of horn feeding, the horn is replaced with equivalent aperture currents by using free space

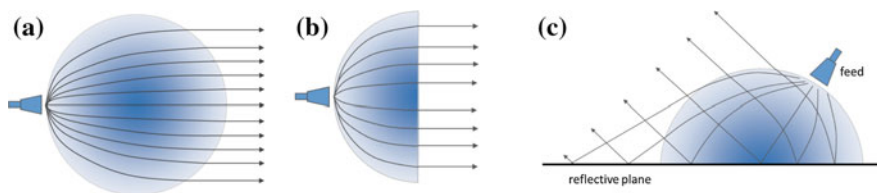


Fig. 2.3 Ray tracing illustration of the properties of **a** Luneburg lens, **b** half Maxwell fisheye lens, **c** hemispherical lens with a ground plane

equivalent principle [8]. For example, if the rectangular horn is used, the field at the horn aperture in the local coordinate system is

$$\mathbf{E}(x, y) = \hat{x} E_0 \cos \left(\frac{\pi y}{W_y} \right) e^{-jk[x^2/\rho_x + y^2/\rho_y]/2} \quad (2.13a)$$

$$\mathbf{H}(x, y) = \hat{y} \frac{E_0}{\eta} \cos \left(\frac{\pi y}{W_y} \right) e^{-jk[x^2/\rho_x + y^2/\rho_y]/2} \quad (2.13b)$$

where W_x and W_y are the width of the horn in x - and y -direction, and ρ_x and ρ_y are distances of the centers of radial waveguides from the horn opening. Therefore, the equivalent currents are

$$\mathbf{J}^{eq}(x, y) = \hat{x} \frac{E_0}{\eta} \cos \left(\frac{\pi y}{W_y} \right) e^{-jk[x^2/\rho_x + y^2/\rho_y]/2} \quad (2.14a)$$

$$\mathbf{M}^{eq}(x, y) = \hat{y} E_0 \cos \left(\frac{\pi y}{W_y} \right) e^{-jk[x^2/\rho_x + y^2/\rho_y]/2} \quad (2.14b)$$

Small horns can be approximated with an elementary area (so-called Huygens source [33]) with E - and H -fields equal to

$$\mathbf{E}^{eq}(r_{feed}, \theta, \phi) = \hat{\theta} \frac{\delta(\theta) \delta(\phi) \delta(r - r_{feed})}{r_{feed}^2 \sin \theta} \quad (2.15a)$$

$$\mathbf{H}^{eq}(r_{feed}, \theta, \phi) = \hat{\phi} \frac{\delta(\theta) \delta(\phi) \delta(r - r_{feed})}{\eta r_{feed}^2 \sin \theta}. \quad (2.15b)$$

We can assume that the small horn is located at the $\theta = 0^\circ$ axis with r -coordinate $r = r_{feed}$. The vector-Legendre transformation of all described models can be found almost completely analytically (for the rectangular horn numerical integration in θ -direction is needed, or alternatively one can consider the array of electric and magnetic dipoles as explained in [13]). For example, the vector-Legendre transformation of the Huygens source is equal

$$\tilde{\mathbf{J}}^{eq}(r_{feed}, n, m = \pm 1) = -\frac{1}{8\pi\eta r_{feed}^2} \frac{2n+1}{n(n+1)} \begin{bmatrix} 0 \\ 1 \\ jm \end{bmatrix} \quad (2.16a)$$

$$\tilde{\mathbf{M}}^{eq}(r_{feed}, n, m = \pm 1) = -\frac{1}{8\pi r_{feed}^2} \frac{2n+1}{n(n+1)} \begin{bmatrix} 0 \\ -jm \\ 1 \end{bmatrix} \quad (2.16b)$$

Note that only the terms with $m = \pm 1$ are different from zero.

Rigorous model, based on closing the feed antenna in a small volume and representing the near-field distribution via spherical harmonics, was presented in [15]. The idea is to project the equivalent current distribution (at the interface of a volume that encloses the source) on the spherical wave basis

$$a_{mn} = -\frac{k^2\eta}{\pi(1+\delta_m)} \cdot \frac{1}{S(n,m)} \int_V \left[\mathbf{J}^{eq} \cdot \mathbf{M}_{mn} - \frac{j}{\eta} \mathbf{M}^{eq} \cdot \mathbf{N}_{mn} \right] dV, \quad (2.17a)$$

$$b_{nm} = -\frac{k^2\eta}{\pi(1+\delta_m)} \cdot \frac{1}{S(n,m)} \int_V \left[\mathbf{J}^{eq} \cdot \mathbf{N}_{nm} - \frac{j}{\eta} \mathbf{M}^{eq} \cdot \mathbf{M}_{nm} \right] dV, \quad (2.17b)$$

where δ_m is the Krönecker symbol. The equivalent electric and magnetic currents are determined mostly from computed data. However, in order to implement the proposed method, details of the feeding antenna structure should be known in order to determine the equivalent currents (e.g., by a general EM solver), which is not always the case—one often receives only the far-field measurements from the antenna manufacturer.

In many cases it is beneficial to use a feed model which is based on spherical mode representation of a far-field radiation pattern of the feed antenna and then using an efficient way of connecting fields in local and global coordinate systems. With this a fast and accurate method for analyzing spherical stratified lens antenna systems can be obtained. Note that the arbitrary feed antenna for which we want to find the model can be characterized either by measurements (often performed by the manufacturer) or by analysis using general EM solver. The proposed feed model contains three steps.

First step

The far-field of the feed antenna can be simply represented using vectorial spherical harmonics [7]:

$$\mathbf{E} = -\sum_n \sum_m a_{mn} \mathbf{M}_{mn} + b_{mn} \mathbf{N}_{mn}, \quad (2.18)$$

where the functions \mathbf{M}_{mn} and \mathbf{N}_{mn} are defined in Eqs. (2.3a)–(2.3b).

Second step

The spherical harmonics representation of the feed antenna is given in the local coordinate system, so we need to rewrite it in the global coordinate system. If we make a translation and/or rotation of the coordinate system, a new basis can be defined with respect to the new coordinate system, and any of the considered functions has to be expressed in the new basis. From addition theorems we get expansion coefficients for \mathbf{M}_{mn} and \mathbf{N}_{mn} in terms of \mathbf{M}'_{mn} and \mathbf{N}'_{mn} which are referenced to the second coordinate system

$$\mathbf{M}_{mn} = \sum_{v=0}^{\infty} \sum_{\mu=-v}^v \left(A_{\mu v}^{mn} \mathbf{M}'_{\mu v} + B_{\mu v}^{mn} \mathbf{N}'_{\mu v} \right), \quad (2.19a)$$

$$\mathbf{N}_{mn} = \sum_{v=0}^{\infty} \sum_{\mu=-v}^v \left(A_{\mu v}^{mn} \mathbf{N}'_{\mu v} + B_{\mu v}^{mn} \mathbf{M}'_{\mu v} \right), \quad (2.19b)$$

where $A_{\mu v}^{mn}$ and $B_{\mu v}^{mn}$ are coefficients that connect the global and local coordinate systems [34, 35]. A way to efficiently calculate them will be discussed at the end of this section.

Third step

The excitation field is rewritten in terms of equivalent currents (suitable for implementation into the code for analyzing spherical multilayer structures [8]):

$$\begin{aligned} \mathbf{J}_{eq} &= (-\hat{\mathbf{r}}) \times \mathbf{H} \\ \mathbf{M}_{eq} &= \mathbf{E} \times (-\hat{\mathbf{r}}) \end{aligned} \quad (2.20)$$

The equivalent currents have the following form in the spectral domain (for example $\tilde{\mathbf{M}}_{eq}$):

$$\begin{aligned} \tilde{\mathbf{M}}_{eq} = & - \sum_n \sum_m \left[a_{mn} \left(\sum_{v=0}^{\infty} \sum_{\mu=-v}^v \sqrt{2\pi S(n, m)} \left(A_{\mu v}^{mn} \hat{\phi} + B_{\mu v}^{mn} \hat{\theta} \right) \right) \right. \\ & \left. + b_{mn} \left(\sum_{v=0}^{\infty} \sum_{\mu=-v}^v \sqrt{2\pi S(n, m)} \left(B_{\mu v}^{mn} \hat{\phi} + A_{\mu v}^{mn} \hat{\theta} \right) \right) \right] \end{aligned} \quad (2.21)$$

Field representation in local and global coordinate systems.

In order to simplify mathematical description of the electromagnetic field distribution it is desirable to expand field solutions in different coordinate sets which describe the same space. The connection between different representations is made by using addition theorems, i.e., by using formulas which describe representation of a basis set of one coordinate system in terms of a basis set of one other [34]. There is a practical problem with calculating coupling coefficients, in particular with the Gaunt coefficients. This was first achieved by Stein [34] in terms of the Wigner 3jm symbols, and *it turns out to be very complicated and lengthy task* [10] (for this reason no results were shown in [10] that are obtained using transformation from local to global coordinate systems).

Coupling coefficients can be efficiently calculated for special case when the center of the local coordinate system is located at the z -axis (which is our case; multiple sources can be easily treated by rotating the coordinate system [36, 37]). In that case the coupling coefficients in Eqs. (2.19a), and (2.19b) are calculated from expressions

$$A_{mv}^{mn} = (-1)^m j^{v-n} \frac{2v+1}{2v(v+1)} \sum_p i^{-p} [n(n+1) + v(v+1) - p(p+1)] \times a(m, n | -m, v | p) z_p(kr_{feed}) \quad (2.22)$$

$$B_{mv}^{mn} = (-1)^m j^{v-n} \frac{2v+1}{2v(v+1)} \sum_p i^{-p} [-2jmk r_{feed}] \times a(m, n | -m, v | p) z_p(kr_{feed}), \quad (2.23)$$

where $a(m, n | \mu, v | p)$ are Gaunt coefficients for which efficient recursion formulas exist for translation in the z -direction (i.e. for $\mu = -m$, see [38] for details).

2.3.2 Examples of Spherical Multi-shell Lens Antennas

12-layer Luneburg lens antenna

To demonstrate the results of the presented methodology, let us consider a 12-shell Luneburg lens antenna developed at EPFL [12]. The lens parameters are given in Table 2.1. The operating frequency is 10 GHz. The outer radius of the lens antenna is 15.9 cm, therefore the antenna is approximately $10\lambda_0$ in diameter. As a feed antenna let us consider a rectangular horn for which the radiation pattern is expanded in spherical harmonics. The opening of the rectangular horn is 2.0×3.0 cm and the horn is placed at $h = 2.3$ cm distance from the lens surface, see [12] for details.

Table 2.1 Lens geometry and electrical characteristics

Shell number	EPFL		Univ. of Rennes		
	Radius (cm)	Permittivity	Shell number	Radius (cm)	Permittivity
1	3.755	1.93	1	8.2	1.92
2	5.52	1.74	2	11.6	1.76
3	7.41	1.71	3	14.2	1.61
4	8.38	1.65	4	16.4	1.46
5	9.415	1.63	5	18.4	1.31
6	9.94	1.56	6	20.0	1.15
7	11.84	1.54			
8	12.5	1.50			
9	13.4	1.40			
10	14.27	1.28			
11	15.15	1.20			
12	15.9	1.10			

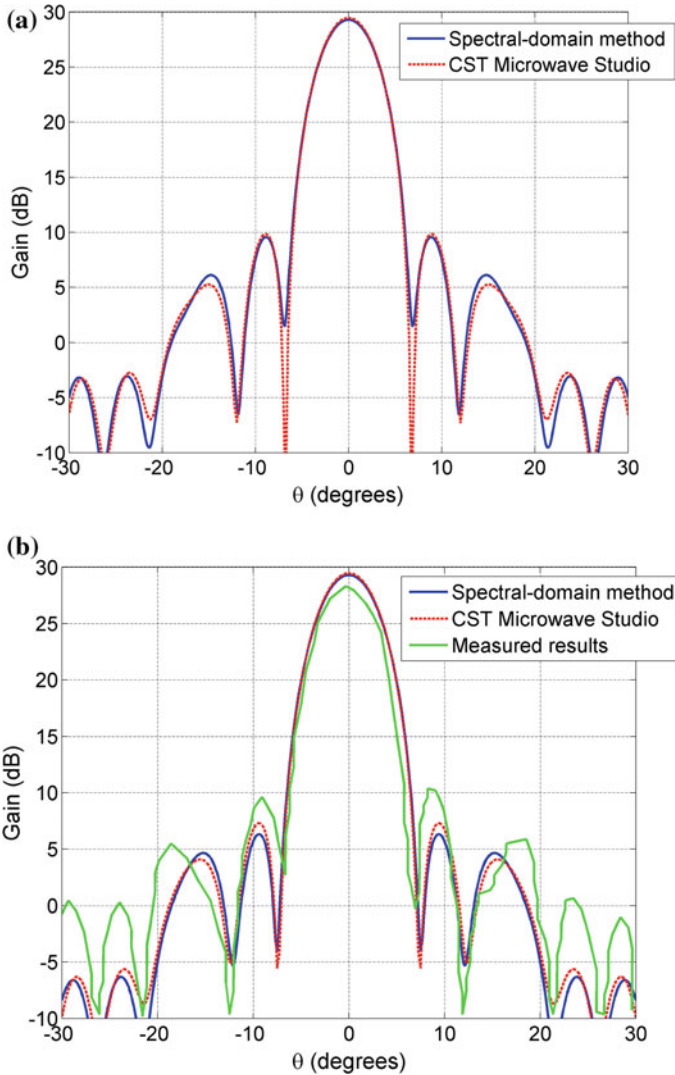


Fig. 2.4 Comparison of the calculated and measured radiation patterns of the 12-layer Luneburg lens antenna developed at EPFL. **a** E-plane, **b** H-plane

The comparison of the calculated radiation pattern of the whole lens antenna with measurements is given in Fig. 2.4. Two analysis methods are compared—the considered analysis method (the presented feed model + G1DMULT algorithm) and results obtained using CST Microwave Studio [39]. There is an excellent agreement between calculated results obtained by two analysis methods. Furthermore, the comparison between calculated results and measurements is also very good. In [12] only the H-plane measurements were provided; this is the reason

why there are no measured results in Fig. 2.4a. For this specific antenna, the spherical wave expansion approach is more than four orders of magnitude faster comparing to the time needed for CST calculations. Therefore, the developed program is suitable for coupling with a global optimization algorithm (e.g. with the Particle Swarm Optimization (PSO) algorithm) to allow synthesis of spherically stratified lens antennas [18].

6-layer Luneburg lens antenna

As a second test example, a six-shell Luneburg lens antenna developed at University of Rennes is considered [14, 15]. The lens parameters are also given in Table 2.1. The operating frequency is 6 GHz, i.e., the lens diameter is $8\lambda_0$. The feeding antenna is simply a waveguide opening with directivity 7.4 dBi placed at distance $h = 1.0$ cm distance from the lens surface. Figure 2.5 shows comparison of the measured and calculated far-field pattern obtained by our method and by the general electromagnetic solver (CST Microwave Studio [39]). The agreement between CST results and spherical harmonic representation is excellent, and with very good agreement with measurements. Here we have also tested two feed models (the one based on far-field radiation pattern and the rigorous one based on projecting the equivalent currents on the spherical wave basis [15]), and the difference between results obtain by using two feed models is negligible (therefore, the results obtained by both feed models are represented with the same line in Fig. 2.5 —spectral domain method).

The analyzed examples of step-index realization of Luneburg lens antenna are two rare examples for which all antenna parameters are given in the open scientific literature (to the best knowledge of the authors, only two additional examples can be found in open scientific literature in [40, 41]). In most of the cases, only a short description of the realized lens is given (e.g., in [42] it is simply stated “8-inch diameter, ten-step Styrofoam lens at 16.65 GHz”).

2.3.3 Multi-shell Lens Optimization

When designing the lens antenna usually there are a lot of parameters to be determined. Since the proposed algorithms for analyzing the lens antenna are very fast it is practical to connect the developed algorithm with some global optimization routine, for example with the Particle Swarm Optimization (PSO) algorithm. This is an evolutionary algorithm similar to the genetic algorithm and to the simulated annealing, but it operates on a model of social interaction between independent agents and utilizes swarm intelligence to achieve the goal of the optimization problem. It is rather easy and straightforward to implement into the program [43], and its performance is at least comparable to the widely used genetic algorithms [44]. All the optimizations done in this chapter were made using the PSO algorithm.

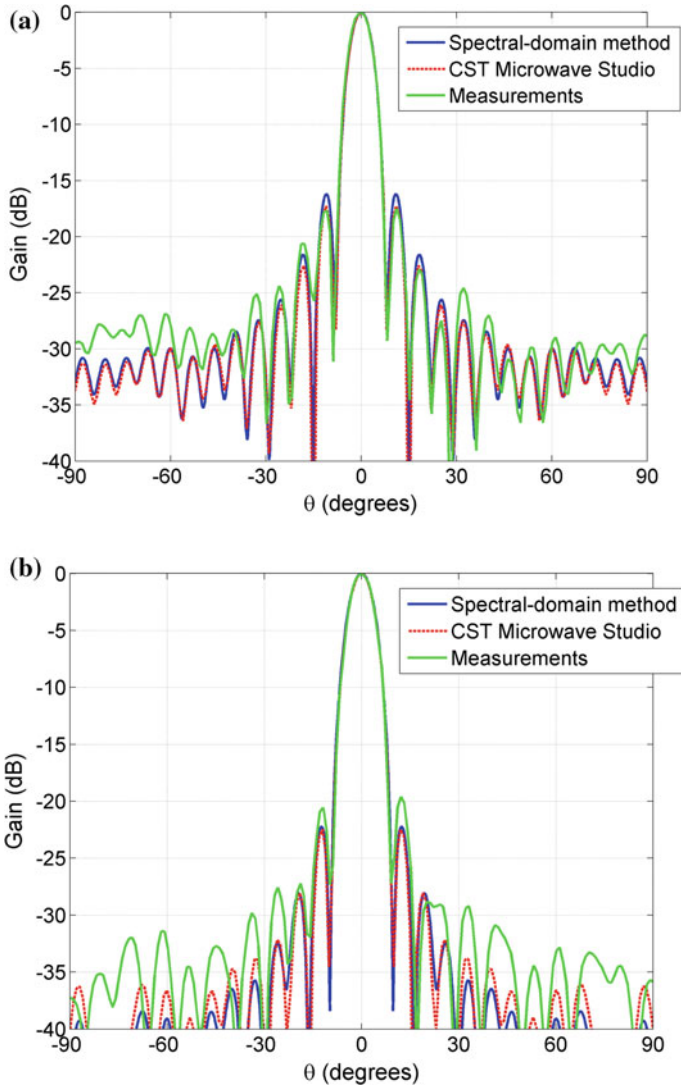


Fig. 2.5 Comparison of the calculated and measured radiation patterns of the 6-layer Luneburg lens antenna developed at University of Rennes. **a** E-plane, **b** H-plane

Characterization of lens and feed antenna

The original Luneburg lens antenna with the permittivity variation $\varepsilon_r(r) = 2 - (r/r_{lens})^2$ has the feed antenna optimally positioned at the lens surface [1]. For practical reasons, it is desirable to move the feed position from the lens surface, i.e., to introduce a gap between the feed and the lens. In order to optimize the lens antenna for new feed position, a modified lens design should be applied [45, 46]

$$\varepsilon_r(r) = \left(1 + \sqrt{1 - \varepsilon_r(r/r_{\text{feed}})^2}\right) \cdot \exp\left(-\frac{2}{\pi} \int_1^{r_{\text{feed}}} \frac{\arcsin(t \cdot r_{\text{lens}}/r_{\text{feed}})}{\sqrt{t^2 - \varepsilon_r(r/r_{\text{lens}})^2}} dt\right), \quad (2.24)$$

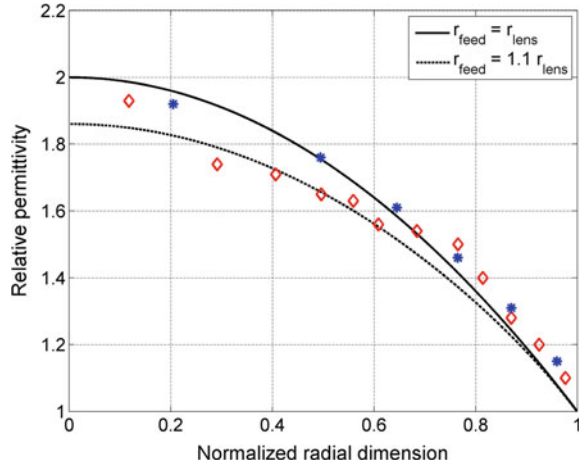
where r and r_{feed} represents the radial coordinate inside the lens and the position of the feed, respectively. Figure 2.6 shows the optimal permittivities of Luneburg lens as a function of normalized radial coordinate in case if the feed is placed at the lens surface ($r_{\text{feed}} = 1.0 \cdot r_{\text{lens}}$) and if it is placed at $1.1 \cdot r_{\text{lens}}$. Manufactured antenna is always realized from several layers of material with constant permittivity. In other words, the practical realization is just a stepwise approximation of the ideal lens. The theoretical curves are compared to permittivities of two manufactured lenses, with the permittivity value of each layer shown for a radius corresponding to the middle of the considered layer $((r_{i-1} + r_i)/2)$. It can be seen that in both cases there is some uncertainty about the obtained electromagnetic parameters of the realized lens antennas. We address this issue at the end of this section (see Fig. 2.8).

In order to study the effect of feed distance from lens surface and the directivity of feed antenna on total directivity of lens antenna and sidelobe levels, we model an “ideal” type of feed antenna, where the far-field is approximated with a cosine type of pattern

$$\mathbf{E}(r, \theta, \phi) = E_0 \frac{e^{-jkr}}{r} \left[\hat{\theta}(\cos(\theta/2))^{q1} \cos \phi - \hat{\phi}(\cos(\theta/2))^{q2} \sin \phi \right]. \quad (2.25)$$

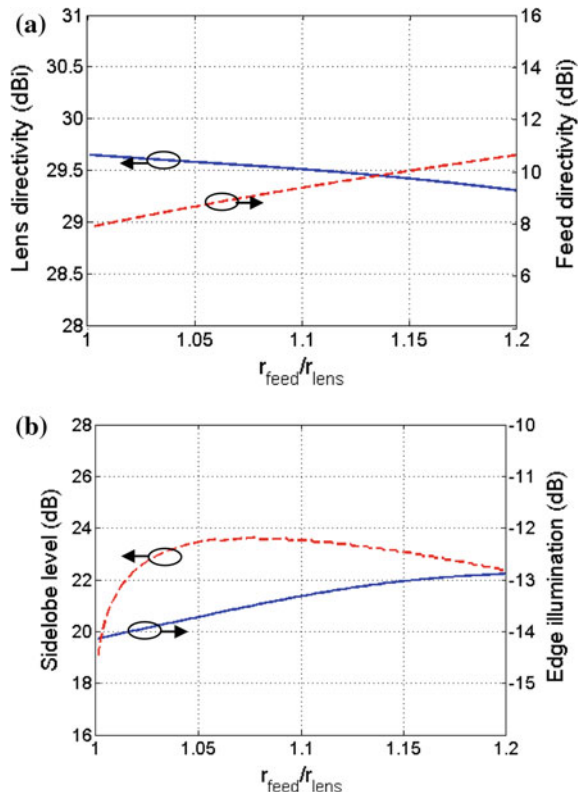
With varying factors $q1$ and $q2$ we can model different types of feed antennas. We have selected $(\cos(\theta/2))^q$ type of function (instead of the $(\cos \theta)^q$ dependence [47]), since it better approximates the low-directivity antennas which are usually

Fig. 2.6 Comparison of permittivity of practical lens realizations and ideal designs for $r_{\text{feed}} = r_{\text{lens}}$ (Luneburg lens) and for $r_{\text{feed}} = 1.1 \cdot r_{\text{lens}}$; diamonds (\diamond)—lens antenna from EPFL, stars ($*$)—lens antenna from University of Rennes



used as feeding elements of lens antennas (some authors have applied $(\cos(\theta/2))^q$ dependency for reflector antenna analysis as well [33]). Similar results can also be obtained using a complex Huygens source [48, 49]. First step in antenna system characterization is to determine the optimum directivity of feeding antenna as a function of feed position r_{feed} . We have calculated directivity of modified Luneburg lens antenna (permittivity variation is obtained using Eq. (2.24); the continuous permittivity variation is approximated with 20-layer step-wise distribution) for different q values, i.e., for different directivities of feeding antenna (Fig. 2.7a). For simplicity, we have taken $q_1 = q_2 = q$. The diameter of the considered lens antenna is $10 \lambda_0$. The optimum directivity of the feed antenna is between 8 and 10 dBi (depending on the designed antenna position r_{feed}), and the directivity of the whole lens antenna does not vary much by moving the feed antenna away from the lens surface (for larger $r_{\text{feed}}/r_{\text{lens}}$ a more directive feed should be used). Therefore, the low-directive horn antennas or waveguide openings are very good elements for feeding the Luneburg lens antennas. In Fig. 2.7b the dependence of sidelobe level and illumination of the edge of the lens antenna is shown for the optimized case. Both, the sidelobe level and edge illumination, do not vary much with the change of feed position; they are around 22 dB and -13 dB, respectively. It is interesting to

Fig. 2.7 **a** Optimized feed directivity and complete lens antenna directivity as a function of the feed antenna position. **b** Sidelobe level and edge illumination of the optimized case. The diameter of the considered Luneburg lens antenna is 10λ (reproduced with permission from Ref. [19])



note that the edge illumination is approximately 3 dB lower comparing to the rule-of-thumb value for reflector antennas (−10 dB edge illumination [47]).

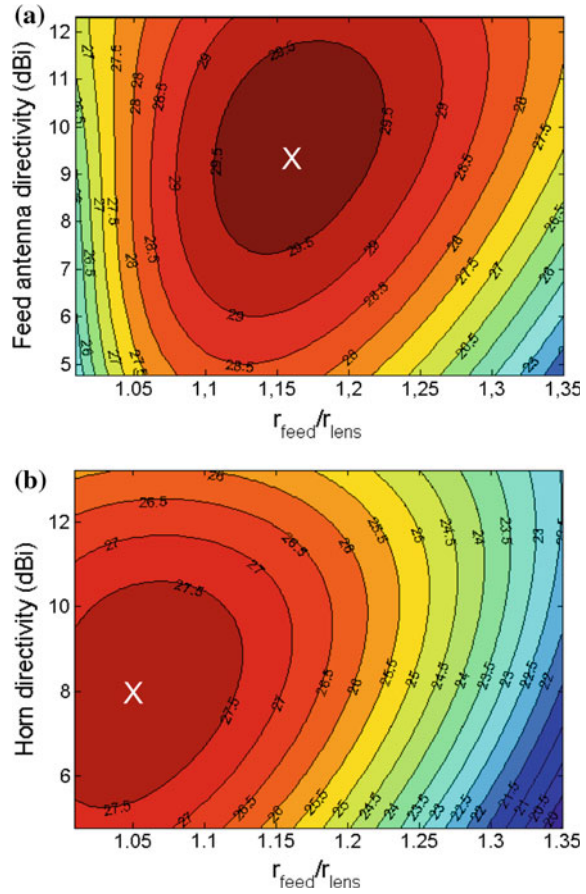
To show the effect of feed selection and placement on a practical realization of Luneburg lens we have calculated the total lens antenna directivities as a function of the feed directivity and position for the two considered realizations (see Table 2.1). Due to uncertainties about the obtained electromagnetic parameters of the realized lens antennas (see Fig. 2.6), it is advisable to make such characterization, i.e., to optimize the feed type as well as its position. Results are shown in Fig. 2.8. It can be seen that there is a significant freedom in selecting the feed antenna type and position for optimal performance. This is in particular important since the phase center of the feed antenna is usually located inside the antenna. In the EPFL case the used horn antenna has 9 dBi directivity and the normalized feed position is $r_{\text{feed}} = 1.145 \cdot r_{\text{lens}}$. The obtained sidelobe level and lens edge illumination is 19.5 dB and around −10 dB, respectively, which is comparable with the optimized feed properties. Similar result is also obtained for the antenna developed at University of Rennes. The used waveguide opening has directivity of 7.4 dBi and the normalized feed position is $r_{\text{feed}} = 1.05 \cdot r_{\text{lens}}$. The directivity determined by the spherical wave expansion technique equals 27.6 dBi whereas 27.5 dBi are predicted by CST. The obtained sidelobe level and lens edge illumination is 16.5 dB and between −6.0 dB (E-plane) and −11.3 dB (H-plane), respectively, which is also comparable to the optimized feed properties.

2.3.4 Fabrication and Experimental Results

The challenge of producing gradient index (GRIN) lenses is already mentioned in the articles of James Clerk Maxwell. Spherical Luneburg lenses have been fabricated using various techniques. Crushed Styrofoam was used to build 186 identical wedges—the lens was sliced through the North–South axis and the gradient variation of index of refraction is obtained by compressing Styrofoam pieces [50]. Polystyrene powder, solidified in heated hemispherical molds, was used to build 10-layer step-index Luneburg lens [40]. Ten-layer step-index Luneburg lenses were also built from Styrofoam and Foamed glass [41, 42]. The needed variation of the refractive index can in addition be obtained by drilling holes in the dielectric structures, which can be easily fabricated by using the traditional printed circuit board technique [51, 52]. Recently, a rapid prototyping machine was used to build a Luneburg lens in X-band by changing the size of plastic blocks centered on the junctions of the plastic rod frame [53].

Lens antennas are attractive solutions for many applications due to their focusing properties, capability of beam scanning, ability to form multiple beams and broadband behavior. For example, spherical lens antennas can be used for automotive radars [28], satellite communications [30, 31], for systems that require communication or/and multiple object tracking through a shared aperture [54], radar cross-section (RCS) enhancers [29], or for astronomy applications [32]. One

Fig. 2.8 Lens antenna directivity as a function of feed position and directivity. The optimum selection that results with the lens antenna with maximum directivity is marked with X. The parameters of the lens antennas are given in Table 2.1; **a** lens antenna from EPFL, **b** lens antenna from University of Rennes (reproduced with permission from Ref. [19])



of the most attractive applications is satellite communication systems for receiving signals from multiple satellites [30]. With this application in mind, a very useful variation of the Luneburg lens antenna is the hemispherical lens in conjunction with the ground plane. Furthermore, this is also an attractive solution for satellite communications with moving vehicles (e.g., trains, see Fig. 2.3c). If applied on the train, the antenna is mounted on the roof of the train and the mechanical system for positioning the feed antenna enables Internet connection via satellite [31]. Also, an important application of the Luneburg lens is a radar cross-section (RCS) enhancer, realized by placing a reflecting cap on the lens surface [29]. An incoming plane wave is focused at a point on the cap and reflected; it is transmitted in the opposite direction after propagating through the lens the second time. By this, a broadband calibrated scatterer with wide angular coverage is obtained, which is needed for calibrating scattered field measurement systems.

Since the construction of multilayer lenses is not easy, for many applications a constant- n lens or a two-layer lens is proposed that is much easier to construct

comparing to Luneburg lenses. For fabrication of optimum constant-index lenses, a material with permittivity of 3.5 is desired, which can be obtained using slip-cast fused silica with small additions of rutile ($\epsilon_r = 90$) [55]. An investigation on the construction of two layer-lenses with off-the-shell materials was performed in [31], where the considered materials were Rexolite ($\epsilon_r = 2.53$), polyethylene ($\epsilon_r = 2.28$) and Fused silica ($\epsilon_r = 3.8$).

Finally, there is a class of two-dimensional Luneburg lenses where the focusing of electromagnetic waves is obtained inside a parallel-plate waveguide. The lens effect can be obtained by changing the thickness of the dielectric plate [56, 57], by drilling holes in a dielectric slab to control the effective permittivity [58], or by printing metallic patterns on dielectric substrate (i.e., variation of index of refraction is obtained using the metasurface concept [59–61]). Recently, the new implementation consisting of two mirrored metallic holey metasurfaces, having ultra-wideband lens property, was introduced [62].

2.4 Cylindrical Multi-shell Lenses

Circular-cylindrical dielectric lenses are attractive antennas because they allow launching multiple fan-beams, each of them originating from one primary feed. Like in the spherical case, the beams can be scanned by moving mechanically the feed around the lens surface or by switching between the feeds. They are also inherently wideband antennas. Such radiation characteristics are of particular interest for many applications at millimeter waves, like Doppler-weather radar, aircraft landing system or imaging systems. These lens antennas have been mostly neglected in the open literature, in contrast to the spherical ones.

In the past, research has been limited to homogeneous cylindrical lenses [63] and cylindrical Luneburg lenses [56, 57] placed between parallel-plate waveguides, i.e., the effect of the finite lens height is not present in this case. There has also been some research regarding antennas with different directivities in two orthogonal planes based on cylindrical Luneburg lens [64], and similar concept has been applied for automotive radars [65]. Cylindrical lenses with special requirements on radiation pattern have also been analyzed as an EM missile launcher, i.e., case when the decay of the energy per unit length is slower than $1/r$ [66]. Finally, the influence of the whispering-gallery modes on obtained directivity of cylindrical Luneburg lens antennas has been studied in [67]. In this section design of multilayered cylindrical dielectric lens antennas of finite height is discussed (a detailed study made by University of Rennes and University of Zagreb is given in [68]).

2.4.1 Lens Geometry

The generic lens antenna configuration is represented in Fig. 2.9a (the lens antenna geometry will be described using the classical cylindrical coordinate system (r, ϕ, z)). It consists of a multilayer cylindrical dielectric lens illuminated by a feed antenna. The total lens height and radius are labeled h and r_{lens} , respectively. The multilayer lens structure is schematized in Fig. 2.9b. The relative permittivity and thickness of layer $\#i$ are labeled $\epsilon_{r,i}$ and a_i , respectively ($1 \leq i \leq N$). Without loss of generality we have selected a pyramidal horn as a feed antenna. The horn (of length L) is fed by a standard metallic rectangular waveguide linearly polarized along z -axis and d denotes the distance separating the horn aperture ($W_y \times W_z$) from the lens boundary.

The multilayer cylindrical lens can be approximated with an infinite circular cylinder. In that case we can apply the method of analysis described in the previous section, this time for cylindrical structures. The major advantage of this method of analysis is that the determination of the lens radiation performance is extremely fast. As a consequence, the iterative full-wave optimization or synthesis of cylindrical lenses can be made in reasonable amount of time. For lenses of moderate size (around $10 \times \lambda_0$ in diameter), the G1DMULT-based program needs less than one second to compute the three-dimensional far-field radiation patterns, whereas general-purpose commercial software like CST Microwave Studio® [39] requires approximately one hour, depending on the lens height and permittivity of the dielectric layers.

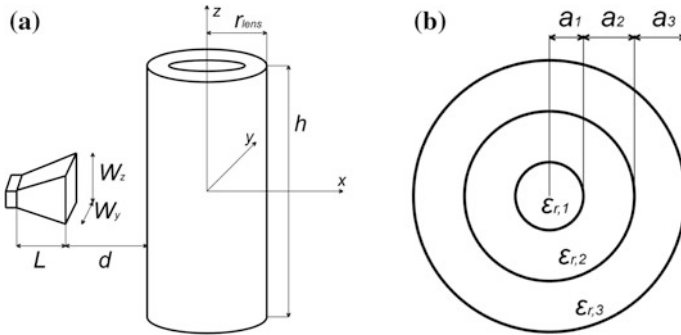


Fig. 2.9 Geometry of the circular-cylindrical dielectric lens antenna. **a** 3-D view. h , r_{lens} , and d denote the lens height, the total lens radius, and the distance between the horn aperture ($W_y \times W_z$) and the lens surface, respectively. L is the length of the horn. **b** Cross-section view of the lens. Definition of the thickness a_i and permittivity $\epsilon_{r,i}$ of each layer

2.4.2 Range of Validity of Modal Analysis Approach

By essence the modal analysis approach assumes that the cylindrical structures are infinitely long, whereas, in practice, the objective is to minimize the height of the antenna prototype while keeping the lens radiation characteristics close to those of an infinite lens. To determine the range of validity of modal analysis approach, we have carried out an exhaustive parametric study consisting in comparing the far-field radiation patterns of a set of lenses analyzed using both the G1DMULT-based program and CST Microwave Studio®.

An empirical formula has been derived to estimate the minimum cylindrical lens height h_{\min} that would provide, in far-field zone, nearly the same results as for lenses of infinite height

$$h_{\min} = 2(2r_{\text{lens}} + d) + W_z \quad (2.26)$$

Here r_{lens} is the total lens radius, d is the distance separating the horn aperture from the lens, and W_z is the height of the feed horn. The formula has been verified for low permittivity materials ($\epsilon_{r,i} < 3$) as, for our applications, there was no need to use materials with even higher permittivities. The validity of this relation is clearly demonstrated in Fig. 2.10 where the fan-beam pattern of an infinite lens at 30 GHz is compared to the radiation patterns of three finite lenses ($h = h_{\min}$, $h = 0.7 \times h_{\min}$, $h = 0.5 \times h_{\min}$). In cases where the lens height is too small, both bases of the cylinder start to contribute to the antenna pattern. This results in a slight variation of the antenna gain, and in strongly pronounced ripples in E-plane.

2.4.3 Numerical and Experimental Results

The objective of the optimization problems studied here is to maximize the antenna gain while keeping low sidelobe levels. The corresponding fitness function is defined as

$$\text{Fitness} = \alpha \cdot \text{Gain} - \beta \cdot SL(H) - \gamma \cdot SL(E). \quad (2.27)$$

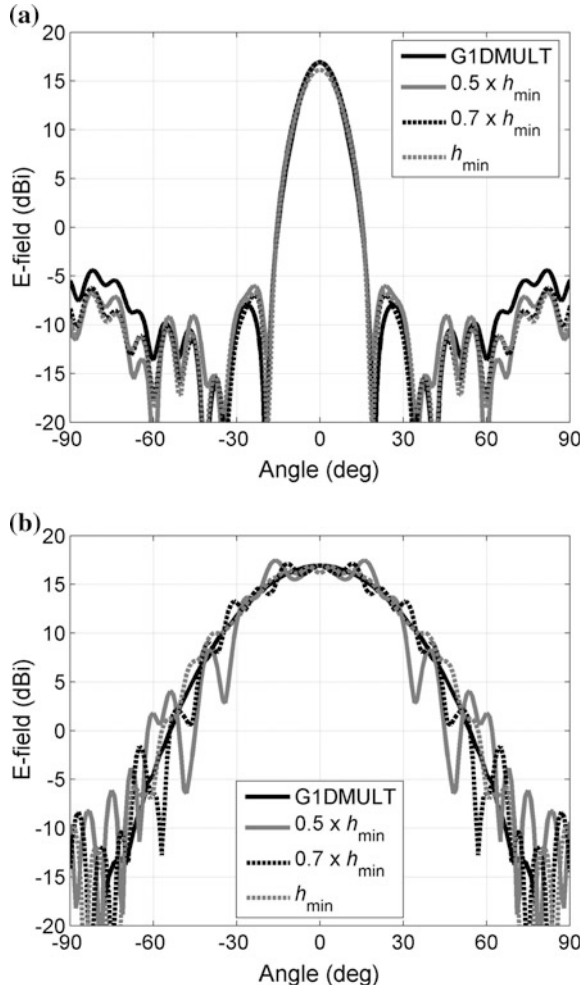
Here *Gain* is the antenna gain at broadside (i.e., along x-axis), and $SL(H)$ and $SL(E)$ are the highest sidelobe levels in the H- and E-planes, respectively. All quantities are expressed in dB. α , β , and γ are weighting coefficients that can be tuned to maximize the gain, or produce fan-beam with low sidelobes. Their typical values are 1, 0.3, and 0.2, respectively. In all cases, the feed and lens parameters are optimized simultaneously since this approach has been shown to be powerful [69].

Influence of the number of layers on the radiation characteristics of small lenses

To the authors' knowledge, in contrast to multilayer spherical lenses (e.g., [14]), there are very few papers dealing with the influence of number of layers on the

Fig. 2.10 Range of validity of modal analysis approach. Comparison of the radiation patterns computed at 30 GHz with G1DMULT and CST Microwave Studio[®].

a H-plane. **b** E-plane. The lens is made in Teflon ($\epsilon_{r,l} = 2.1$, $r_{lens} = a_l = 2.86$ cm) and is illuminated by a pyramidal horn fed by a standard WR-28 waveguide ($L = 2$ cm, $W_y = 2.4$ cm, $W_z = 1$ cm, $d = 0.65$ cm)



radiation characteristics of a cylindrical lens (see, e.g., [67]). The study described here is restricted to lenses with a moderate gain (~ 18 dBi). Their total diameter is equal to 5 cm, i.e., $5 \times \lambda_0$, at 30 GHz. The lens and feed horn parameters have been optimized simultaneously, and the number of layers was varied from 1 to 3. The range of variation of the optimization parameters are the following: $0.05 \text{ cm} \leq d \leq 2 \text{ cm}$, $0.4 \text{ cm} \leq W_z \leq 2 \text{ cm}$, $0.8 \text{ cm} \leq W_y \leq 3 \text{ cm}$, $0.5 \text{ cm} \leq L \leq 3 \text{ cm}$, $1.4 \leq \epsilon_{r,i} \leq 5$, $\forall i = 1, \dots, 3$. Both the gain and the sidelobe level were optimized ($\alpha = 1$, $\beta = 0.3$, $\gamma = 0.2$).

Up to seven optimization runs per lens configuration were launched, and the best result was selected based on the value of the fitness function and the visual inspection of the far-field radiation patterns. The geometry of the best designs and their corresponding patterns in H- and E-planes are given in Table 2.2 and

Table 2.2 Influence of the number of layers

	1 layer	2 layers	3 layers
Layer no. 1: thickness (cm)	2.50	0.10	0.73
Layer no. 1: permittivity	1.43	1.56	1.93
Layer no. 2: thickness (cm)	–	2.40	0.72
Layer no. 2: permittivity	–	1.52	1.77
Layer no. 3: thickness (cm)	–	–	1.05
Layer no. 3: permittivity	–	–	1.63
d (cm)	0.82	0.77	0.63
W_z (cm)	1.05	1.03	1.07
W_y (cm)	2.82	2.66	1.57
L (cm)	3.00	2.84	3.00
Gain (dBi)	17.76	17.63	17.62
Sidelobes (dB)	–22.30	–22.95	–23.71

Fig. 2.11, respectively. The radiation characteristics of the best three lens configurations are nearly identical. This demonstrates that there is no need to use more than one layer to optimize the fan-beam characteristics of moderate-sized cylindrical lenses.

Experimental results

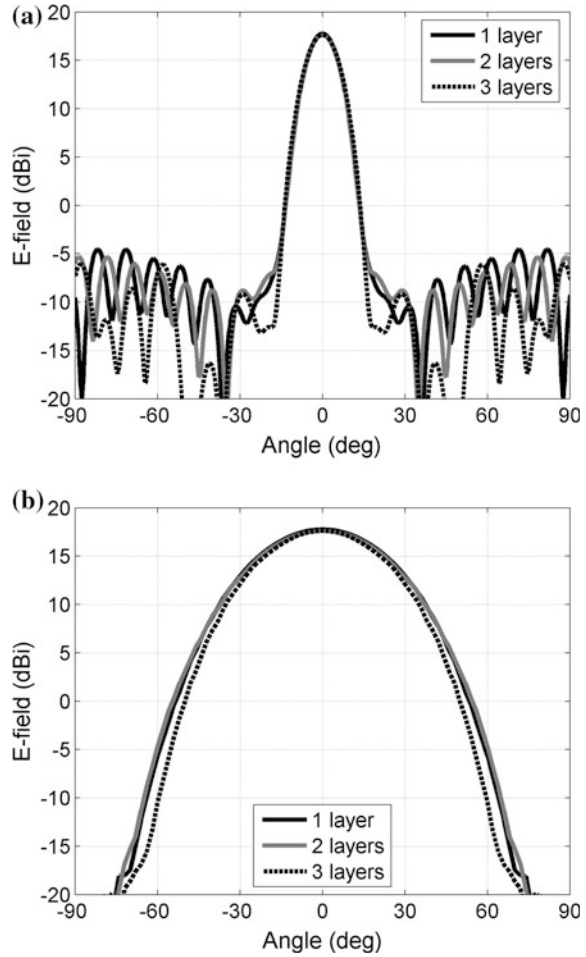
To validate experimentally the previous results, a single-layer homogeneous cylindrical lens has been optimized in Ka-band. In this case, the results given in Table 2.2 suggest using a bulk material whose dielectric constant equals 1.43. Although customized materials are available commercially or could be synthesized using effective medium theory [51, 58] their fabrication cost remains very expensive.

To keep the antenna manufacturing as simple as possible, a cylindrical lens made from Teflon ($\epsilon_{r,1} = 2.1$) has been synthesized. The final dimensions of the antenna prototype are the following: $r_{\text{lens}} = a_1 = 2.82$ cm, $L = 2$ cm, $W_z = 1$ cm, $W_y = 2.4$ cm, and $d = 0.65$ cm. The minimum height h_{min} of the lens, guarantying that the infinite and finite lenses have nearly the same radiation characteristics, is equal to 13.6 cm (according Eq. (2.26)).

To keep some margin with respect to this threshold value, a 16 cm long lens was manufactured. As the optimized dimensions of the feed horn are not standard, a specific horn was fabricated in aluminum using electrical discharge machining techniques. Both the lens antenna and the feed horn were fabricated and measured at IETR, University of Rennes [68].

The radiation patterns measured at 30 GHz in H- and E-planes are represented in Figs. 2.12a, b, respectively. They are in excellent agreement with those predicted by G1DMULT-based program and CST Microwave Studio[®], confirming thereby the relevance of the empirical relation (2.26). Additional measurements have been performed from 26 to 40 GHz (Fig. 2.13). They show that the lens patterns are very stable over the whole frequency band proving that the design is wideband.

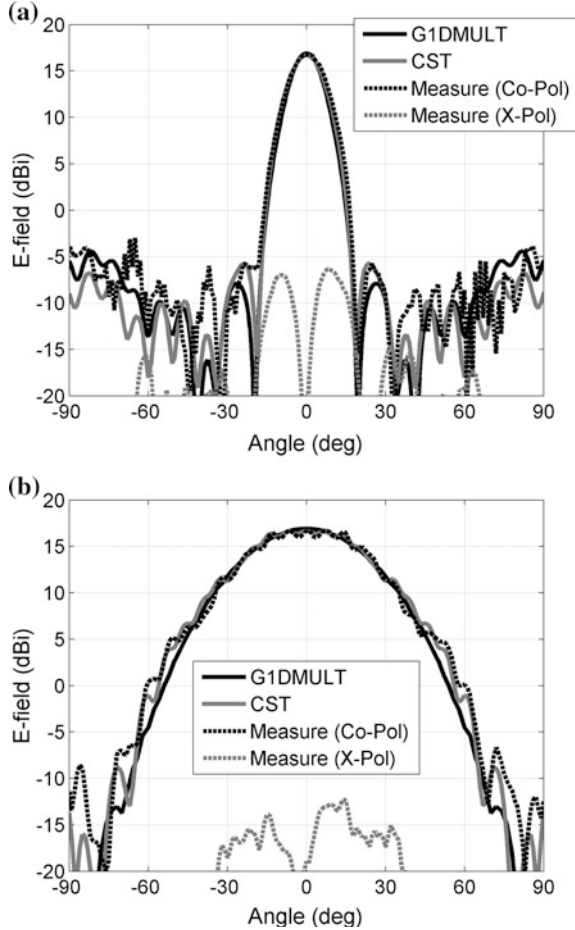
Fig. 2.11 Radiation patterns of the best designs at 30 GHz. The patterns have been computed using G1DMULT-based program. **a** H-plane. **b** E-plane. The corresponding lens geometries are detailed in Table 2.2



2.4.4 Size Reduction

Cylindrical lenses whose height is defined according to Eq. (2.26) produce nearly the same fan-beam patterns as lenses of infinite height. Nevertheless, applying this empirical criterion leads to large and bulky lens configurations. To overcome this limitation, the lens geometry has been optimized to minimize the influence of both lens bases, in particular to reduce the substantial ripples that are generated in E-plane for lenses of small height (Fig. 2.10b). These ripples originate from longitudinal resonant modes that contribute significantly to radiation in E-plane. This phenomenon is clearly highlighted on the amplitude near-field map represented in Fig. 2.14.

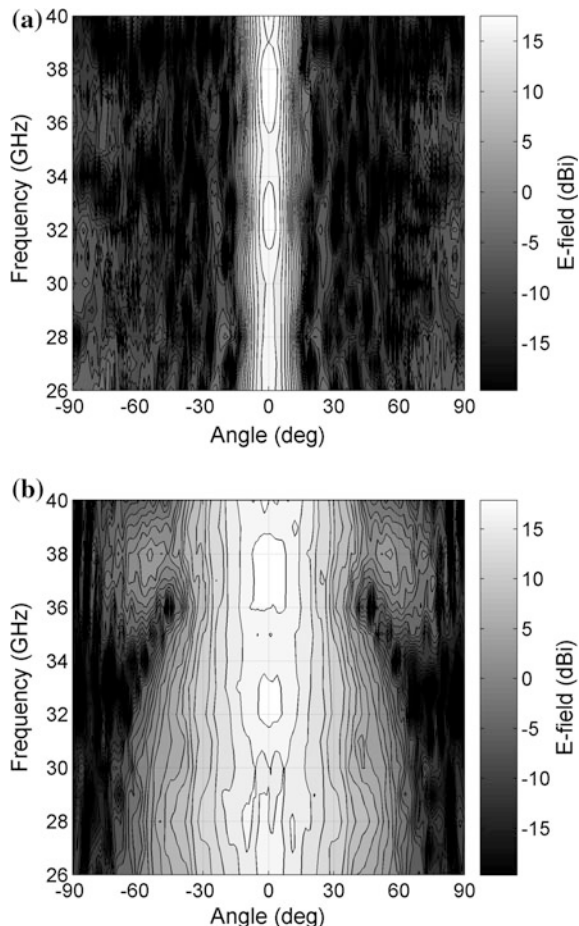
Fig. 2.12 Synthesized lens made from Teflon: radiation patterns measured and computed at 30 GHz.
a H-plane. **b** E-plane



In order to reduce as much as possible the effects of lens truncation, two conical shapes are added to the cylinder bases (Fig. 2.15). As the resulting lens shape is rotationally symmetric, the ability to launch multiple beams and scan them around the lens axis is maintained. The height and permittivity of both cones are labeled h_c and $\epsilon_{r,c}$, respectively. Their permittivity must be higher than the one of the cylindrical part of the lens to prevent possible total reflection that can happen when electromagnetic waves travels from a denser to a less dense medium.

Two cones made in Rexolite ($\epsilon_{r,c} = 2.53$) have been designed to improve the radiation characteristics of the small lens represented in Fig. 2.15a. The height of the circular-cylindrical part is 4.8 cm. The lens is illuminated by the same horn as in Sect. 2.4.3. The cone height has been optimized using CST Microwave Studio® to minimize the ripple levels in E-plane ($h_c = 2$ cm). As a result the total antenna height equals 8.8 cm.

Fig. 2.13 Synthesized lens made in Teflon: radiation patterns measured in Ka-band. **a** H-plane. **b** E-plane. These patterns are quite frequency independent



The radiation patterns computed at 30 GHz are represented in Fig. 2.16, and they are compared to those of two pure cylindrical lenses: the first one has the same height (8.8 cm) as the lens with conical caps, and the height of the second one (16 cm) fulfills relation (2.26). The three lenses have nearly the same patterns in H-plane (Fig. 2.16a). However, by introducing two conical caps at the bases of small circular-cylindrical lenses, the ripple level in E-plane can greatly be reduced (Fig. 2.16b). This technique also provides a faster roll-off, compared to pure cylindrical lenses. The influence of cones on the amplitude near-field distribution is highlighted in Fig. 2.14b. It can be seen that the waves can propagate into the denser cone (without total reflection) and finally in the surrounding air as they approach the Rexolite-Air boundary at smaller incident angles.

The lens with conical caps has been fabricated and measured at University of Rennes [68]. Both cones have been assembled on the cylinder bases using a thin film of dielectric glue. The distance d separating the feed horn and the lens surface

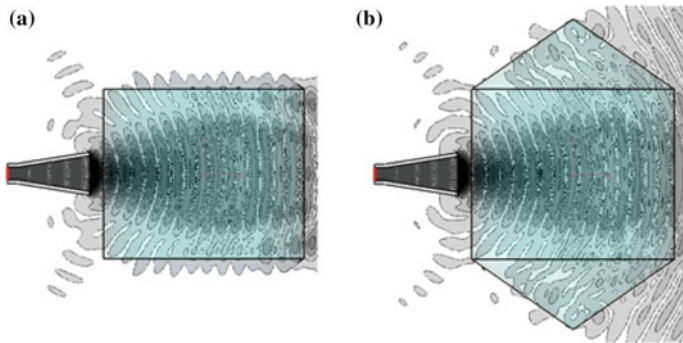


Fig. 2.14 Amplitude near-field maps (arbitrary units). **a** Original design. The lens parameters are the same as for the experimental model (Sect. 2.4.3), except the lens height that is roughly three times smaller than h_{\min} ($h = 4.8$ cm). **b** Proposed design. The lens is the same as in **(a)** with addition of two cones. The cone parameters are the following: $h_c = 2$ cm, $\epsilon_{r,c} = 2.53$

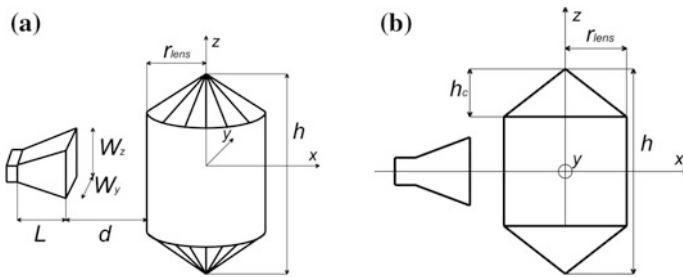
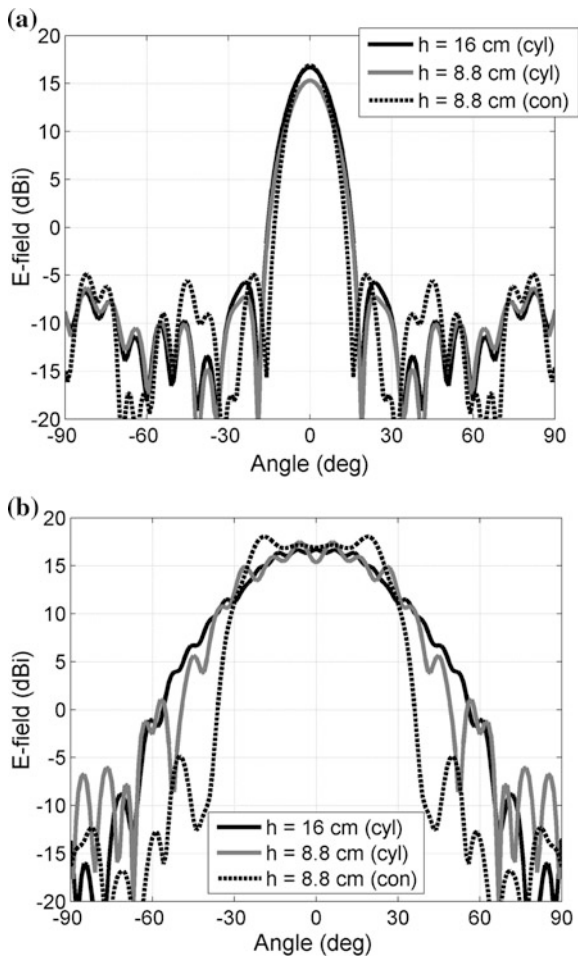


Fig. 2.15 Reduced-height circular-cylindrical dielectric lens with conical caps. The lens is illuminated by a pyramidal feed horn linearly polarized along z -axis. **a** 3-D view. **b** Cross-section view

is equal to 0.4 cm. The radiation patterns measured in both principal planes at 30 GHz are represented in Fig. 2.17. The agreement between numerical and experimental results is excellent, especially in E-plane where the ripple level in the main beam is smaller than 1.5 dB. The cross-polarization level is smaller than -21 dB and the measured antenna gain equals 17.66 dBi.

The height reduced design is also wideband as can be seen in Fig. 2.18. Measurements performed from 26 to 40 GHz show that the radiation patterns are really frequency independent over Ka-band with an expected increase of the gain as operating frequency increases. It should be noted that height reduced design shows even higher insensitivity of the radiation pattern to change in frequency compared to the original circular-cylindrical design.

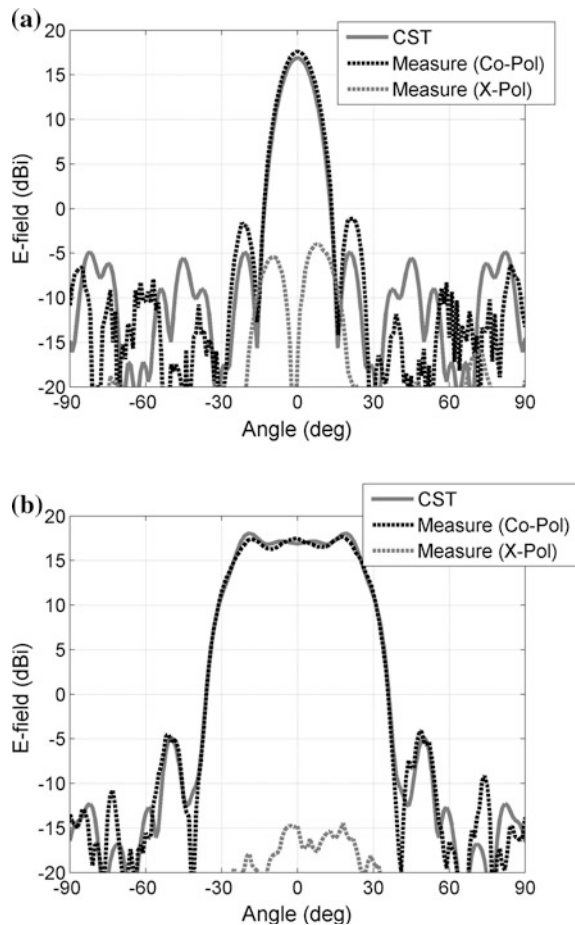
Fig. 2.16 Radiation patterns (computed at 30 GHz) of the reduced-size Teflon lens ($h = 8.8$ cm, $\epsilon_{r,1} = 2.1$) with conical caps ($h_c = 2$ cm, $\epsilon_{r,c} = 2.53$). Comparison with two pure cylindrical Teflon lenses of variable height ($h = 8.8$ cm or 16 cm). **a** H-plane. **b** E-plane. All lenses have the same radius ($r_{\text{lens}} = a_1 = 2.82$ cm) and are illuminated by the same horn as in Sect. 2.4.3



2.5 Concluding Remarks

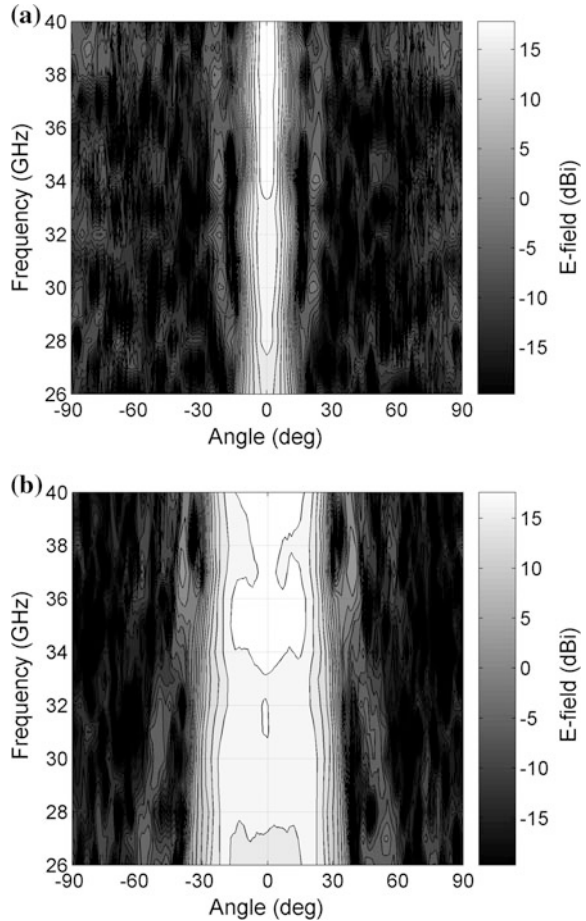
A fast and reliable synthesis method is presented for designing multilayered spherical and circular-cylindrical dielectric lens antennas. In order to make the analysis program fast, thus enabling efficient merging with the global optimization routine, the multi-shell lens structure is analytically taken into account using Green's functions approach. The proposed analysis approach can successfully analyze lens structures with arbitrary number of layers and arbitrary type of excitation antenna. The latter is obtained by representing the measured or calculated far-field radiation pattern in terms of spherical harmonics in local coordinate system.

Fig. 2.17 Reduced-height Teflon lens with conical caps from Rexolite: radiation patterns measured and computed at 30 GHz. **a** H-plane. **b** E-plane



In the cylindrical case, the analysis approach assumes that the cylindrical structure is infinitely long, so we assess the range of validity of the analysis method. An empirical formula to estimate the minimum cylindrical lens height that provides similar far-field to the lens of infinite height is derived. For the cases where the lens size should further be reduced, a new height-reduction technique is proposed. It consists in adding conical caps to both bases of the cylinder. This technique allows a significant reduction of the ripple level in the elevation pattern of small cylindrical lenses, leading to high-quality fan-beams. Theoretical predictions are successfully verified by fabricating and characterizing various lens prototypes.

Fig. 2.18 Reduced-height Teflon lens with conical caps made in Rexolite: radiation patterns measured in Ka-band. **a** H-plane. **b** E-plane. The radiation pattern is quite similar at all frequencies, with expected gain increase as frequency increases (reproduced with permission from Ref. [68])



References

1. R.K. Luneburg, *Mathematical Theory of Optics* (Brown University Press, Providence, RI, 1944)
2. E. Braun, Radiation characteristics of the spherical Luneberg lens. *IRE Trans. Antennas Propag.* **4**(2), 132–138 (1956)
3. S.P. Morgan, Generalizations of spherically symmetric lenses. *IRE Trans. Antennas Propag.* **7**(4), 342–345 (1959)
4. T.L. Ap Rhys, The design of radially symmetric lenses. *IEEE Trans. Antennas Propag.* **18**(5), 497–506 (1970)
5. G. Godi, R. Sauleau, D. Thouroude, Performance of reduced size substrate lens antennas for millimeter-wave communications. *IEEE Trans. Antennas Propag.* **53**(4), 1278–1286 (2005)
6. A.D. Greenwood, J.-M. Jin, Finite-element analysis of complex axisymmetric radiating structures. *IEEE Trans. Antennas Propag.* **47**(8), 1260–1266 (1999)
7. J.A. Stratton, *Electromagnetic Theory* (McGraw Hill, New York, 1941)
8. R.F. Harrington, *Time Harmonic Electromagnetic Fields* (McGraw Hill, New York, 1961)

9. J.J. Mikulski, E.L. Murphy, The computation of electromagnetic scattering from concentric spherical structures. *IEEE Trans. Antennas Propag.* **11**, 169–177 (1963)
10. H. Mieras, Radiation pattern computation of a spherical lens using Mie series. *IEEE Trans. Antennas Propag.* **30**(6), 1221–1224 (1982)
11. S.S. Vinogradov, E.D. Vinogradova, P.D. Smith, Accurate modelling of a scanning Luneburg lens antenna Mie series approach, in *Proceedings of the International Conference on Electromagnetics in Advanced Applications, Turin, Italy, Sep. 1999* (1999), pp. 277–280
12. J.R. Sanford, Spherically Stratified Microwave Lenses, Ph.D. Thesis No. 1065, *École polytechnique fédérale de Lausanne (EPFL)*, 1992
13. J.R. Sanford, Scattering by spherically stratified microwave lens antennas. *IEEE Trans. Antennas Propag.* **42**, 690–698 (1994)
14. B. Fuchs, L. Le Coq, O. Lafond, S. Rondineau, M. Himdi, Design optimization of multishell Luneburg lenses. *IEEE Trans. Antennas Propag.* **55**, 283–289 (2007)
15. B. Fuchs, S. Palud, L. Le Coq, O. Lafond, M. Himdi, S. Rondineau, Scattering of spherically and hemispherically stratified lenses fed by any real source. *IEEE Trans. Antennas Propag.* **56**, 450–460 (2008)
16. W.C. Chew, *Waves and Fields in Inhomogeneous Media* (Van Nostrand Reinhold, New York, 1990)
17. H. Mosallaei, Y. Rahmat-Samii, Non-uniform Luneburg and 2-shell lens antennas: radiation characteristics and design optimization. *IEEE Trans. Antennas Propag.* **49**, 60–69 (2001)
18. T. Komljenovic, Z. Sipus, J.-P. Daniel, Scanning vehicular lens antennas for satellite communications, in *Proceedings of EuCAP'2010, Barcelona, Spain* (2010), pp. 1–4
19. Z. Sipus, D. Bojanjac, T. Komljenovic, Electromagnetic modeling of spherically stratified lenses illuminated by arbitrary sources. *IEEE Trans. Antennas Propag.* **63**(4), 1837–1843 (2015)
20. S. Rondineau, Modélisation de lentilles sphériques à gradient d'indice et sources conformes associées, Ph.D. dissertation, *University of Rennes 1, Rennes, France, Dec. 2002*
21. S. Rondineau, A.I. Nosich, J.-P. Daniel, M. Himdi, S.S. Vinogradov, MAR analysis of a spherical-circular printed antenna with finite ground excited by an axially symmetric probe. *IEEE Trans. Antennas Propag.* **52**(5), 1270–1280 (2004)
22. Z. Sipus, N. Burum, S. Skokic, P.-S. Kildal, Analysis of spherical arrays of microstrip antennas using moment method in spectral domain. *IEE Proc. Microw. Antennas Propag.* **153**, 533–543 (2006)
23. Z. Sipus, S. Skokic, M. Bosiljevac, N. Burum, Study of mutual coupling between circular stacked-patch antennas on a sphere. *IEEE Trans. Antennas Propag.* **56**, 1834–1844 (2008)
24. Z. Sipus, P.-S. Kildal, R. Leijon, M. Johansson, An algorithm for calculating Green's functions for planar, circular cylindrical and spherical multilayer substrates. *Appl. Comput. Electromagn. Soc. J.* **13**, 243–254 (1998)
25. L.B. Felsen, N. Marcuvitz, *Radiation and Scattering of Waves* (Prentice-Hall Inc., New Jersey, 1973)
26. W.Y. Tam, K.M. Luk, Resonances in spherical-circular microstrip structures of cylindrical-rectangular and wraparound microstrip antennas. *IEEE Trans. Microw. Theory Tech.* **39**, 700–704 (1991)
27. B. Fuchs, O. Lafond, S. Palud, L. Le Coq, M. Himdi, M.C. Buck, S. Rondineau, Comparative design and analysis of Luneburg and Half Maxwell fish-eye lens antennas. *IEEE Trans. Antennas Propag.* **56**, 3058–3062 (2008)
28. B. Schoenlinner, X. Wu, J.P. Ebling, G.V. Eleftheriades, G.M. Rebeiz, Wide-scan spherical-lens antennas for automotive radars. *IEEE Trans. Microw. Theory Tech.* **50**(9), 2166–2175 (2002)
29. J.R. Sanford, Analysis of spherical radar cross-section enhancers. *IEEE Trans. Microw. Theory Tech.* **43**(6), 1400–1403 (1995)
30. C.S. Lee, M.E. Rayner, *Luneburg lens antenna with multiple gimbaled RF feeds*, U.S.A. patent No. US 6266029 B1

31. J. Thornton, Wide-scanning multi-layer hemisphere lens antenna for Ka band. *IEE Proc. Microw. Antennas Propag.* **153**(6), 573–578 (2006)
32. A.J. Parfitt, J.S. Kot, G.L. James, The Luneburg lens as a radio telescope element, in *Proceedings of the IEEE Antennas and Propagation Society International Symposium, Salt Lake City* (2000), pp. 170–173
33. P.-S. Kildal, *Foundations of Antennas—A Unified Approach* (Studentlitteratur AB, 2000)
34. S. Stein, Addition theorems for spherical wave functions. *Q. Appl. Math.* **19**, 15–24 (1961)
35. O.R. Cruzan, Translational addition theorems for spherical vector wave functions. *Quart. Appl. Math.* **20**, 33–40 (1962)
36. D.L. Sengupta, T.M. Smith, R.W. Larson, Radiation characteristics of spherical array of circularly polarized elements. *IEEE Trans. Antennas Propag.* **16**, 2–7 (1968)
37. J.R. Sanford, Z. Sipus, Sidelobe reduction with array fed spherical lenses, in *Proceedings of the IEEE Antennas and Propagation Society International Symposium, Newport Beach* (1995), pp. 670–673
38. J.H. Bruning, Y.T. Lo, Multiple scattering of EM waves by spheres. Part I—Multiple expansion and ray optical solutions. *IEEE Trans. Antennas Propag.* **19**, 378–390 (1971)
39. CST Microwave Studio™, *Computer Simulation Technology AG*, www.cst.com, Darmstadt, Germany (2013)
40. G.D.M. Peeler, H.P. Coleman, Microwave stepped-index Luneburg lenses. *IRE Trans. Antennas Propag.* **6**, 202–207 (1958)
41. L.C. Gunderson, J.F. Kauffman, A high temperature Luneburg lens. *IEEE Proc.* **56**, 883–884 (1968)
42. R.E. Webster, Radiation patterns of a spherical luneburg lens with simple feeds. *IRE Trans. Antennas Propag.* **6**, 301–302 (1968)
43. J. Robinson, Y. Rahmat-Samii, Particle swarm optimization in electromagnetics. *IEEE Trans. Antennas Propag.* **52**(2), 397–407 (2004)
44. D.W. Boeringer, D.H. Werner, Particle swarm optimization versus genetic algorithms for phased array synthesis. *IEEE Trans. Antennas Propag.* **52**(3), 771–778 (2004)
45. A.S. Gutman, Modified Luneberg lens. *J. Appl. Phys.* **25**, 855–859 (1954)
46. D.K. Cheng, Modified Luneberg lens for defocused source. *IRE Trans. Antennas Propag.* **8**, 110–111 (1960)
47. Y. Rahmat-Sammii, Reflector antennas, in *Antenna Engineering Handbook*, ed. by J.L. Volakis, Chap. 15 (McGraw-Hill, 2007)
48. V.S. Buligin, T.M. Benson, Y.V. Gandel, A.I. Nosich, Full-wave analysis and optimization of a TARA-like shield-assisted paraboloidal reflector antenna using a Nystrom-type method. *IEEE Trans. Antennas Propag.* **61**(10), 4981–4989 (2013)
49. D. Bojanjac, A.I. Nosich, Z. Sipus, Design of spherical lens antennas using complex Huygens element, in *Proceedings of EuCAP'2014, The Hague, The Netherlands* (2014), pp. 1–3
50. G.P. Robinson, Three-dimensional microwave lens, in *Tele-Tech & Electronic Industry*, Nov. 1954 (1954), p. 73
51. S. Rondineau, M. Himdi, J. Sorieux, A sliced spherical Lüneburg lens. *IEEE Antennas Wirel. Propag. Lett.* **2**, 163–166 (2003)
52. H.F. Ma, B.G. Cai, T.X. Zhang, Y. Yang, W.X. Jiang, T.J. Cui, Three-dimensional gradient-index materials and their applications in microwave lens antennas. *IEEE Trans. Antennas Propag.* **61**, 2561–2569 (2013)
53. M. Liang, W.-R. Ng, K. Chang, K. Gbele, M.E. Gehm, H. Xin, A 3-D Luneburg lens antenna fabricated by polymer jetting rapid prototyping. *IEEE Trans. Antennas Propag.* **62**, 1799–1807 (2014)
54. M.A. Mitchell, J.R. Sandford, Luneburg lens revival, in *Electronics&Wireless World*, May 1989 (1989), pp. 456–458
55. W.R. Free, F.L. Cain, C.E. Ryan Jr., C.P. Burns, E.M. Turner, High-power constant-index lens antennas. *IEEE Trans. Antennas Propag.* **22**, 582–584 (1974)
56. G.D.M. Peeler, D.H. Archer, A two-dimensional microwave Luneburg lens. *IRE Trans. Antennas Propag.* **1**, 12–23 (1953)

57. X. Wu, J. Laurin, Fan-beam millimeter-wave antenna design based on the cylindrical luneburg lens. *IEEE Trans. Antennas Propag.* **55**, 2147–2156 (2007)
58. K. Sato, H. Ujiie, A plate Luneburg lens with the permittivity distribution controlled by hole density. *Electr. Commun. Jpn.* **85**(9), 1–12 (2002)
59. C. Pfeiffer, A. Grbic, A printed, broadband Luneburg lens antenna. *IEEE Trans. Antennas Propag.* **58**, 3055–3059 (2010)
60. S. Maci, G. Minatti, M. Casaletti, M. Bosiljevac, Metasurfing: addressing waves on impenetrable metasurfaces. *IEEE Antennas Wirel. Propag. Lett.* **10**, 1499–1502 (2011)
61. M. Bosiljevac, M. Casaletti, F. Caminita, Z. Sipus, S. Maci, Non-uniform metasurface luneburg lens antenna design. *IEEE Trans. Antennas Propag.* **60**, 4065–4073 (2012)
62. O. Quevedo-Teruel, M. Ebrahimpouri, M.N.M. Kehn, Ultrawideband metasurface lenses based on off-shifted opposite layers. *IEEE Antennas Wirel. Propag. Lett.* **15**, 484–487 (2016)
63. L.C. Gunderson, An electromagnetic analysis of a cylindrical homogeneous lens. *IEEE Trans. Antennas Propag.* **20**, 476–479 (1972)
64. G. Dubost, Flat linear radiating array applied on a cylindrical lens, in *MELECON'85, Madrid, Spain*, vol. 3 (1985), pp. 215–218
65. P. Wenig, R. Weigel, Analysis of a microstrip patch array fed cylindric lens antenna for 77 GHz automotive radar, in *IEEE AP-S International Symposium Digest, San Diego (CA), 5–11 July 2008*
66. T.T. Wu, R.W.P. King, H.-M. Shen, Circular cylindrical lens as a line-source electromagnetic-missile launcher. *IEEE Trans. Antennas Propag.* **37**(1), 39–44 (1989)
67. A.V. Boriskin, A.I. Nosich, Whispering-gallery and Luneburg-lens effects in a beam-fed circularly layered dielectric cylinder. *IEEE Trans. Antennas Propag.* **50**(9), 1245–1249 (2002)
68. T. Komljenovic, R. Sauleau, Z. Sipus, L. Le Coq, Layered circular-cylindrical dielectric lens antennas—synthesis and height reduction technique. *IEEE Trans. Antennas Propag.* **58**(5), 1783–1788 (2010)
69. R. Sauleau, B. Barès, A complete procedure for the design and optimization of arbitrarily-shaped integrated lens antennas. *IEEE Trans. Antennas Propag.* **54**(4), 1122–1133 (2006)

Aperture Antennas for Millimeter and Sub-Millimeter
Wave Applications

Boriskin, A.; Sauleau, R. (Eds.)

2018, X, 490 p. 323 illus., 218 illus. in color., Hardcover

ISBN: 978-3-319-62772-4